THE ACOUSTIC FAR FIELD OF A TURBULENT BOUNDARY LAYER FLOW CALCULTED FROM RANS SIMULATIONS OF THE FLOW

by

Jean-Baptiste Blanc

A Thesis Submitted to the Faculty of

The College of Engineering and Computer Science

in Partial Fulfillment of the Requirements for the Degree of

Master of Science

Florida Atlantic University

Boca Raton, Florida

December 2009

THE ACOUSTIC FAR FIELD OF A TURBULENT BOUNDARY LAYER FLOW CALCULTED FROM RANS SIMULATIONS OF THE FLOW

by

Jean-Baptiste Blanc

This thesis was prepared under the direction of the candidate's thesis advisor, Dr. Stewart A. Glegg, Department of and Ocean and Mechanical Engineering, and has been approved by the members of his supervisory committee. It was submitted to the faculty of the College of Engineering and Computer Science and was accepted in partial fulfillment of the requirements for the degree of Master of Science.

SUPERVISORY COMMITTEE:

Stewart A. Glegg, Ph.D.
Thesis Advisor

Palaniswamy Ananthakrishnan, Ph.D.

Chaouki Ghenai, Ph.D.

Mohammad Ilyas, Ph.D.
Chair, Department of Ocean and Mechanical Engineering

Karl K. Stevens, Ph.D., P.E.
Dean, College of Engineering and Computer Science

Barry T. Rosson, Ph.D.
Dean, Graduate College

Nov. 24, 2009
Date

ACKNOWLEDGEMENTS

Few people helped making this thesis a success, but their role was of critical importance in the process.

I owe my greatest thank to my advisor Dr Glegg for entrusting me with this project and for providing me with this wonderful opportunity. I benefitted of his sharp teaching skills and experience and learned a great deal of knowledge and techniques working for him. He was always patient and provided all insight needed in my research.

I would like to express my deepest gratitude to my fantastic girlfriend who stood by me day after day during such a long time, being so far away and still so close. She knew how to transmit her positive energy to fill me with strength and confidence from the day I left France to the day I receive my degree.

Finally, I am endlessly grateful to my parents and family for their support in a number of ways. They extensively contributed to this achievement through their attention, their implication and their unfailing optimism.

It was a pleasure studying in this environment and I will never thank them enough.

ABSTRACT

Author:	Jean-Baptiste Blanc
Title:	The Acoustic Far Field of a Turbulent Boundary Layer Flow Calculated From RANS Simulations of the Flow.
Institution:	Florida Atlantic University
Thesis Advisor:	Dr. Stewart A. Glegg
Degree:	Master of Science
Year:	2009

Boundary layers are regions where turbulence develops easily. In the case where the flow occurs on a surface showing a certain degree of roughness, turbulence eddies will interact with the roughness elements and will produce an acoustic field. This thesis aims at predicting this type of noise with the help of the Computational Fluid Dynamics (CFD) simulation of a wall jet using the Reynolds Average Navier-Stokes (RANS) equations. A frequency spectrum is reconstructed using a representation of the turbulence with uncorrelated sheets of vorticity. Both aerodynamic and acoustic results are compared to experimental measurements of the flow. The CFD simulation of the flow returns consistent results but would benefit from a refinement of the grid. The surface pressure spectrum presents a slope in the high frequencies close to the experimental spectrum. The far field noise spectrum has a 5dB difference to the experiments.

THE ACOUSTIC FAR FIELD OF A TURBULENT BOUNDARY LAYER FLOW CALCULTED FROM RANS SIMULATIONS OF THE FLOW

LIST OF FIGURES

LIST OF TABLES

CHAPTER 1: INTRODUCTION

1.1. Motivation

Boundary layers are found in any flow over a body and are certainly the hardest part of the flow to consider. Many mechanisms are known to lead to a turbulent flow within this layer, the most important being the inertia forces exceeding the viscous forces. But this phenomenon can be triggered or enhanced by the interaction between roughness elements on the surface of the body and the flow. The acoustic field radiated by this kind of flow is called roughness noise. It is characterized by particularly low energy levels compared to those that can be generated by high Mach number flows such as jets. However roughness noise can create an important contribution to the overall noise in underwater applications thus presenting a critical issue when stealth counts in the design. Measurements of this type of noise require a specific facility and therefore limited experimental data is available. In this thesis we will focus on using Computational Fluid Dynamics (CFD) simulations of a turbulent boundary layer flow over a wall to predict the radiated acoustic far field, thus offering a valuable alternative to the experimental approach.

1.2. Literature review

Due to the very recent improvements in computer capabilities, Computational AeroAcoustics has only become available relatively recently. Most of the articles dealing with this subject were therefore written during the last decade. Although the acoustic analogy developed by Lighthill characterized the problem of sound generation by flow, sound generation by turbulence is still a difficult problem to understand in most practical cases. This is due to the scale of the problem; acoustic waves are propagating at a much higher velocity than the flow while being of 10 orders of magnitude smaller in amplitude. Computational grids to resolve these problems need to be very fine to obtain high numerical accuracy and time steps must be short enough to catch all the information in an acoustic problem involving high frequencies. Also, acoustic waves often propagate over long distances and the computational code's inherent dissipation ensuring stability is incompatible with this characteristic of the problem. The Reynolds Averaged Navier-Stokes (RANS) equations are unable to give a solution to this problem and DNS simulation are typically out of reach for a problem of practical dimensions using a reasonable computation time. Consequenctly LES is a widely used alternative. An alternative solution to resolve the propagation issue is to solve the acoustic sources with a commercial code and then couple the results to an acoustic propagation code.

An illustration of the principle detailed above is given in the study performed by Mathey (2007) where a hybrid zonal RANS-LES model is used to simulate the aerodynamic (broadband and tonal) noise of the flow past an airfoil trailing edge. A LES sub-grid is embedded in the RANS domain and is used to resolve the acoustic sources.

The Ffowcs-Williams and Hawkings equations are used to calculate the far field. In this study, two different ways of generating turbulence at the inlet of the LES domain were assessed, a simple random noise generator versus a synthetic turbulence generator. Results show a better performance of the synthetic turbulence generator when compared to experimental measurements, especially for the separation location and for the amplitude of the trailing edge tonal noise. It was shown that the vortex method gave better results because generating a spatially correlated turbulent flow field, sustaining turbulence and allowing the turbulent flow to recover a three-dimensional state more rapidly. The study showed the critical importance of the turbulence model for this type of predictions.

Lee *et al.* (2005) predicted the frequency spectrum of wall pressure fluctuations by using time-mean flow fields and turbulent flow characteristics obtained from RANS calculations of a flow with a $k-\varepsilon$ model. They used the turbulence kinetic energy to represent the vertical component of the turbulence velocity. The turbulence kinetic energy was assumed to follow an anisotropic distribution and was based on an equilibrium turbulent shear flow. Their result showed a good correlation to experimental data providing the anisotropy assumption.

Spitz (2005) performed a study of two points velocity correlations to predict trailing edge noise. Using data from Direct Numerical Simulations of a channel flow carried out by Moser (1998), one of his conclusions was that the vorticity correlation lengthscale in the direction normal to the wall is only a few percent of the boundary layer thickness.

These studies later led Glegg *et al.* (2008) to the hypothesis that the velocity fluctuations in a turbulent shear flow can be related to the strength of uncorrelated sheets of vorticity as a function of the distance above the wall. They could express the acoustic near field on the surface and the acoustic far field radiated by the trailing edge of an airfoil using RANS calculations of the turbulence kinetic energy in the flow.

1.3. Objectives

The main objective in this study is to use the theory derived by Glegg (2008) with another type of flow than around an airfoil and observe if it is applicable. This thesis aims at predicting the acoustic far field radiated by a turbulent boundary layer of a flow over a rough wall.

Glegg and Devenport (2009) give an equation for the acoustic far field generated by a flow over a rough surface. Their equation requires the surface pressure spectrum on the wall beneath the flow. To obtain this, the procedure developed by Glegg *et al.* (2008) to compute the surface pressure spectrum from RANS calculations of the local Turbulence Kinetic Energy (TKE) in a boundary layer flow can be used.

Thus the project can be outlined in three parts; first, RANS calculations of a wall-bounded jet flow will be performed. Then an existing theory (Glegg *et al.* (2008)) will be implemented to compute the pressure spectrum on the surface. The results, especially the turbulence kinetic energy, from the CFD simulations will be used as input data for this theory. Eventually, the surface pressure spectrum could be plugged in the equation for the acoustic far field spectrum (Glegg and Devenport (2009)). At each one of these steps, a

comparison can be made with the experimental results from a study that was conducted by a team of researchers in the low-noise wall-jet facility of Virginia Tech (Grissom (2007), Alexander (2009)). Experimental data include aerodynamic performances, surface and far field pressure spectra.

CHAPTER 2: SIMULATION OF THE FLOW

This chapter presents the RANS simulations that were made of a wall jet flow and whose results are to be used in the upcoming chapters to predict the radiated far field noise of this flow. Throughout this chapter, we will make reference to the low-noise, low-turbulence wind tunnel facility located in Virginia Tech. This experimental set up was used to perform measurements of the flow we consider in this study. These aerodynamic and acoustic measurements are to be used in the validation process of the work presented in this paper.

2.1. Grid

This first section aims at presenting the grid that was built to conduct this CFD study. As all the results that we will obtain are based on this numerical simulation of the flow and are to be compared to experimental data collected in Virginia Tech, the computational grid is chosen to represent the experimental set-up as accurately as possible. Figure 1 below shows the anechoic facility that was used to carry out the experiments (all dimensions are given in mm).

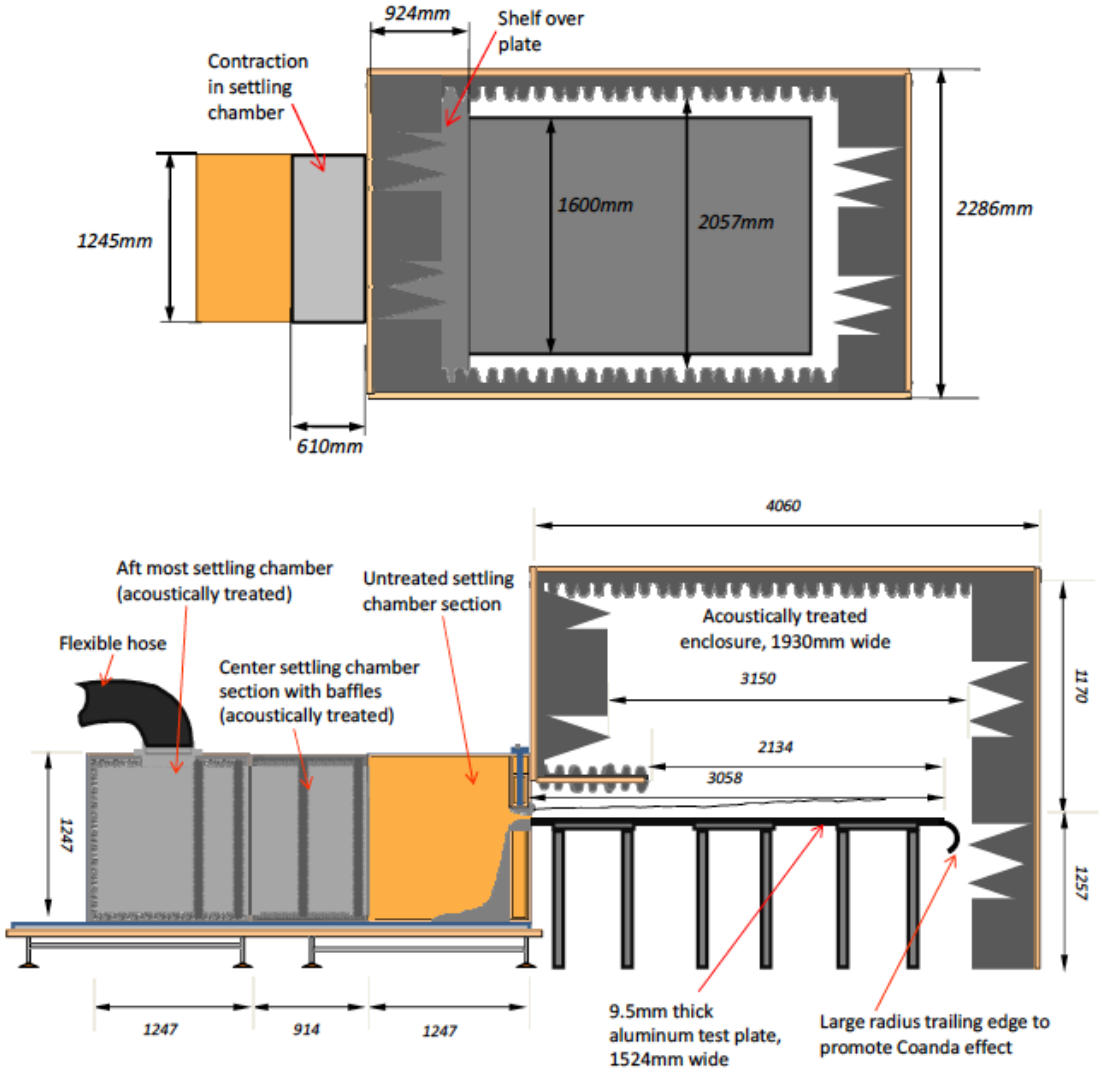

Figure 1: Virginia Tech wall Jet Facility *(reproduction from Alexander, 2009)*

The tunnel produces a 1206mm wide jet over a 3058mm long aluminium plate. The plate was 1600mm wide to contain the jet in a spanwise fashion. The flow is produced by a fan located upstream of the flexible rubber hose designated in the side view of Figure 1. The settling chamber features several acoustically treated baffles blocking direct radiation of sound from the fan though the jet nozzle. To ensure aerodynamic fidelity, the last section

of the acoustic settling chamber will be represented in the computational grid. The nozzle was designed as shown on Figure 2.

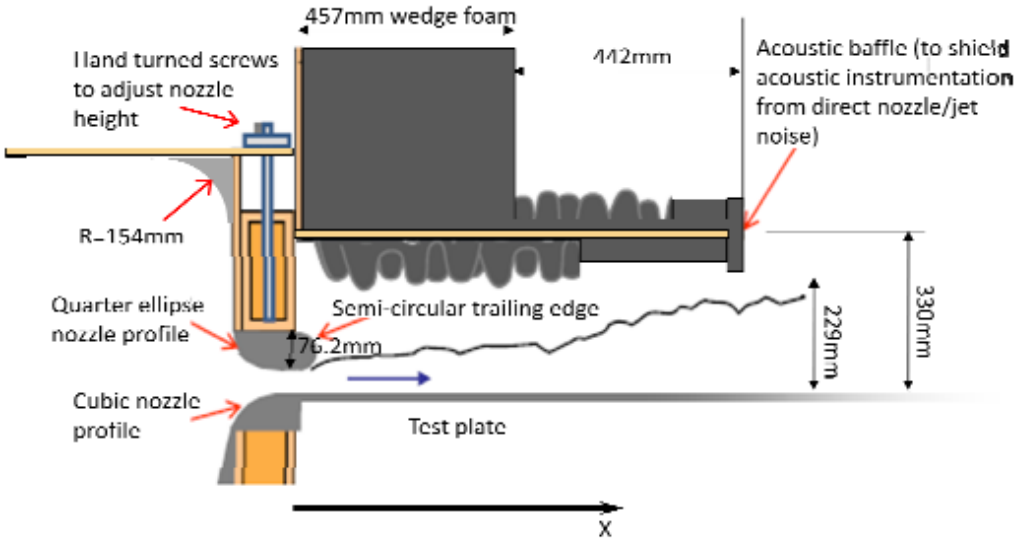

Figure 2: Nozzle section *(reproduction from Alexander, 2009)*

The computational grid will reproduce the 154mm radius on the 90 degrees turn towards the nozzle, the quarter ellipse profile which has a 3:1 aspect ratio and the 76.2mm diameter of the half-cylinder constituting the upper lip of the nozzle which was included to reduce edge noise. The jet nozzle was designed to be adjustable in height and two different heights were tested experimentally. We will take it as constant and equal to 12.7mm. We will also take the trailing edge of the test plate into account (Figure 1). It is made of a 150mm diameter semi circle aiming at promoting a Coanda effect, directing the outflow downwards. The measurement chamber is acoustically treated using 89mm egg crate foam on the upper and sidewalls and 457mm wedges on the leading and trailing walls. However this treatment will not be represented in the numerical model resulting in

a volume of the model slightly larger than the original. The jet was shown to be two-dimensional within 810 mm of span around the centerline and until 1867mm downstream the nozzle. The measurements were taken within this area. Therefore, the numerical study will be carried out in two dimensions, assuming to be in the plane $z = 0$, relatively to a fixed frame whose origin is located in the spanwise center of the nozzle, on the test plate and at the junction between the plate and the lower lip of the nozzle. Another point of interest is the baffle represented in Figure 2. It lies above the nozzle and extends 924mm downstream. It is designed to shield the far field instrumentation from directly radiated jet noise. This artifact will not appear in the numerical model.

The roughness was represented experimentally using aluminum oxide sandpaper and floor sanding sheets with roughness ranging from 220 grit to 20 grit. The roughness fetches were 610mm by 305mm and were spanwise centered on the plate with the shorter dimension running streamwise and their leading edge located at 1257mm downstream the nozzle. The CFD model does not take any roughness into account. This aspect will be developed in details later, in chapter 4.

The geometry and grid were produced using the meshing software ANSYS ICEM CFD. Figure 3 below shows the geometry of the domain that was used to simulate the flow. It features two different regions, the settling chamber damping the turbulence existing in the flow and attenuating the noise radiated by the fan upstream and secondly, the measurement chamber where the wall jet develops.

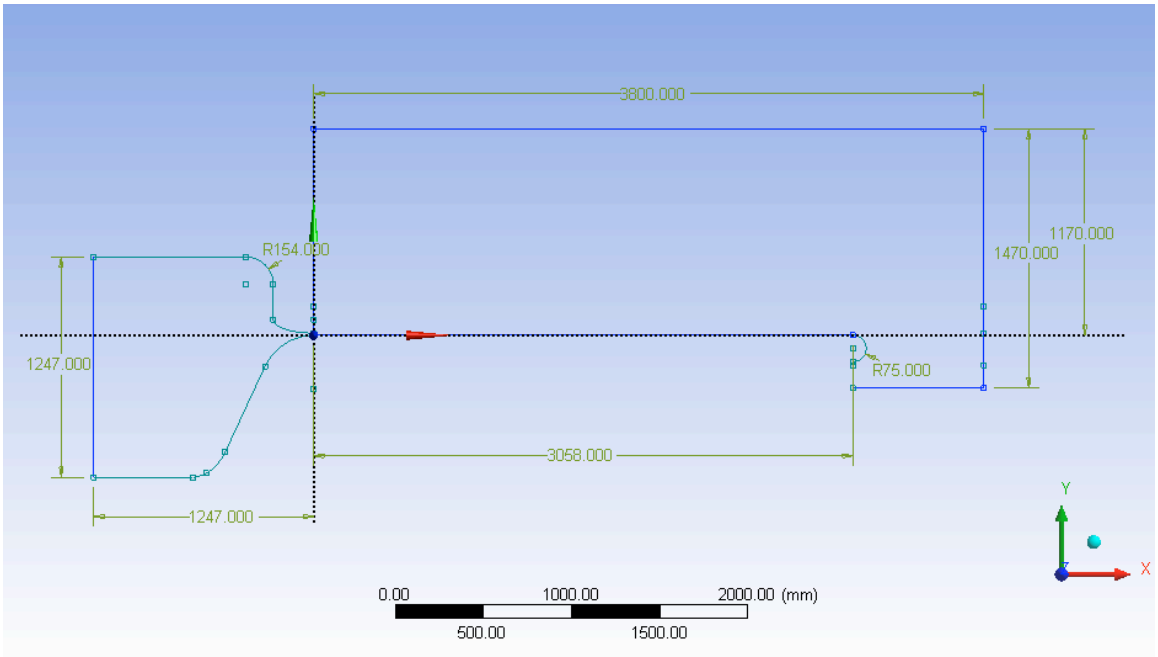

Figure 3: Geometry of the domain

The domain was gridded using an unstructured mesh of 110,000 elements, both triangles and quads. The mesh was made fine in the boundary layer with a resolution of 0.4mm in the closest region to the wall in order to capture the velocity and the turbulence kinetic energy with a good level of accuracy. Elements were bunched also in the regions of the nozzle and at the trailing edge of the test plate to ensure a correct flow.

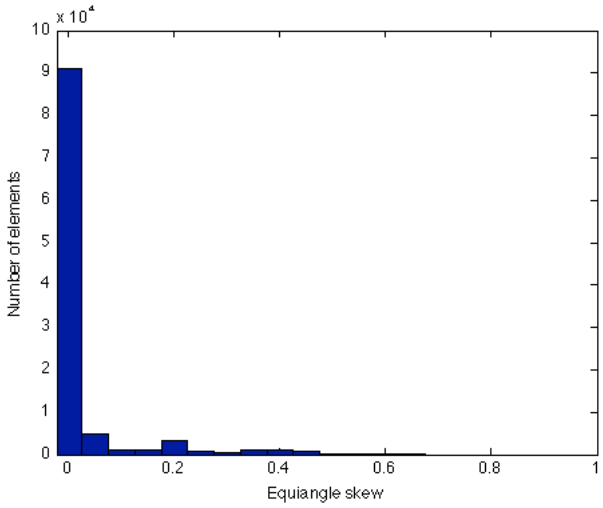

Figure 4: Equiangle skew of the elements

Figure 4 gives an indicator of the quality of the elements. It represents the repartition of the values of the cell equiangle skew. This indicator is defined by the relationship:

Cell equiangle skew = $\max\left[\frac{q_{\max}-q_e}{180-q_e}, \frac{q_e-q_{\min}}{q_e}\right]$ where $q_{\max}$ is the largest angle of the cell, $q_{\min}$ the smallest angle and q_e is the equiangle, *i.e.* 60 for a triangle or 90 for a quad. Therefore, an equiangle skew of 0 reflects a perfectly equiangular cell whereas a skew of 1 indicates a degenerate cell, with almost coplanar nodes. As a general rule, a good mesh does not contain cells with an equiangle skew greater than 0.95, which is the case here since the maximum value is 0.7. It will later appear interesting to have information about the size of the cells at a given profile in the domain. Figure 5 gives the step size or the distance from one node to another plotted versus the distance from the wall at 1352mm downstream the nozzle exit.

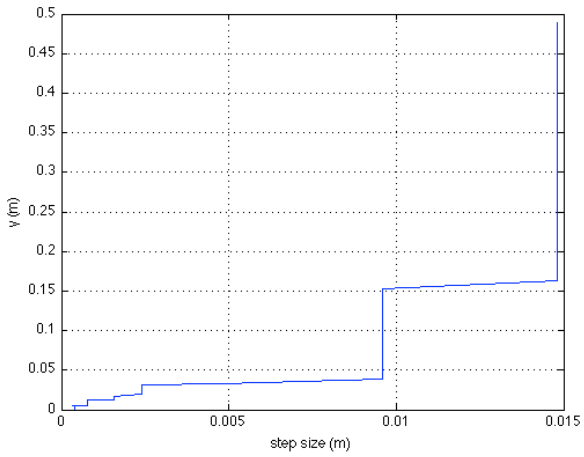

Figure 5: Step size profile at 1352mm downstream the nozzle exit

2.2. Solver

In this section we present the method we used to obtain a solution to the wall-jet flow. We will start by detailing the equations that were solved numerically. This study uses the RANS equations to simulate the flow. These equations are based on the momentum and continuity equations given in Einstein's notation by

$$\tilde{\rho}\left[\frac{\partial \tilde{v}_i}{\partial t}+\tilde{v}_j\frac{\partial \tilde{v}_i}{\partial x_j}\right]=-\frac{\partial \tilde{p}}{\partial x_i}+\frac{\partial \tilde{S}_{ij}}{\partial x_j}$$
$$\left[\frac{\partial \tilde{\rho}}{\partial t}+\tilde{v}_j\frac{\partial \tilde{\rho}}{\partial x_j}\right]+\tilde{\rho}\frac{\partial \tilde{v}_j}{\partial x_j}=0 \qquad (2.2.1)$$

$\tilde{v}_i(\vec{x},t)$ represents the i-th component of the fluid velocity at a certain point in time and space, $\tilde{p}(\vec{x},t)$ is the static pressure an-d $\tilde{S}_{ij}(\vec{x},t)$ the viscous stress tensor. $\tilde{\rho}$ is the density

of the fluid and is assumed to be constant and equal to a mean value ρ_0. The tilde denotes the instantaneous value. Assuming a homogeneous and incompressible flow, these equations reduce to

$$\rho_0\left[\frac{\partial\tilde{v}_i}{\partial t}+\tilde{v}_j\frac{\partial\tilde{v}_i}{\partial x_j}\right]=-\frac{\partial\tilde{p}}{\partial x_i}+\frac{\partial\tilde{S}_{ij}}{\partial x_j}$$
$$\frac{\partial\tilde{v}_j}{\partial x_j}=0 \qquad (2.2.2)$$

The instantaneous values of velocity and pressure involved in these equations can be decomposed following Reynold's decomposition as

$$\tilde{v}_i=U_i+v_i$$
$$\tilde{p}=P+p \qquad (2.2.3)$$
$$\tilde{S}_{ij}=S_{ij}+s_{ij}$$

where the upper-case symbols represent a mean value and the lower-case symbols represent a fluctuation about this mean. If we substitute this decomposition into the governing equations (2.2.2), then take the time-average of these equations, recalling that the time-average of a mean value is the mean value itself, that the time-average of a fluctuating value is zero and that averaging and differentiation commute, equations (2.2.2) become

$$\rho_0\left[\frac{\partial U_i}{\partial t}+U_j\frac{\partial U_i}{\partial x_j}\right]=-\frac{\partial P}{\partial x_i}+\frac{\partial S_{ij}}{\partial x_j}-\rho_0\left\langle v_j\frac{\partial v_i}{\partial x_j}\right\rangle$$
$$\frac{\partial U_j}{\partial x_j}=0 \qquad (2.2.4)$$

The averaged fluctuating terms on the right hand side of the momentum equations will drop to zero or not depending on the correlation of the terms in the product. It generally does not. The continuity equation in (2.2.4) above can be used to imply that $\frac{\partial v_j}{\partial x_j}=0$ and therefore $\left\langle v_i\frac{\partial v_j}{\partial x_j}\right\rangle=0$. This yields that $\left\langle v_j\frac{\partial v_i}{\partial x_j}\right\rangle=\frac{\partial}{\partial x_j}\left\langle v_iv_j\right\rangle$, which used in equation (2.2.4) gives

$$\rho_0\left[\frac{\partial U_i}{\partial t}+U_j\frac{\partial U_i}{\partial x_j}\right]=-\frac{\partial P}{\partial x_i}+\frac{\partial}{\partial x_j}\left[S_{ij}-\rho_0\left\langle v_iv_j\right\rangle\right]$$
$$\frac{\partial U_j}{\partial x_j}=0 \qquad (2.2.5)$$

The term inside the brackets on the right hand side of the momentum equations $\rho_0\left\langle v_iv_j\right\rangle$ is called the Reynolds stresses, even though it is not a stress. However it acts on the flow as if it were. This term is a major issue to be dealt with in a turbulent flow. It introduces more unknowns in the system bringing the total number of unknowns to be larger than the number of equations available. This problem is solved using a turbulence model. Several types of model exist, but in this study we will focus on the two-equation $k-\varepsilon$

model, which is proven to work well for the type of flow considered here. The $k-\varepsilon$ model introduces two new transport equations in the problem that represent the turbulence properties of the flow, one determining the energy of the turbulence in the flow, the second determining its scale. The $k-\varepsilon$ model uses two parameters, the turbulence kinetic energy k and the turbulence dissipation rate ε, which is directly proportional to the lengthscale of the turbulence. The two-equation turbulence models are all based on the Boussinesq hypothesis representing the Reynolds stresses as:

$$-\rho_0\left\langle v_i v_j \right\rangle = \mu_t\left(\frac{\partial U_i}{\partial x_j}+\frac{\partial U_j}{\partial x_i}\right)+\frac{2}{3}\rho_0 k\delta_{ij} \tag{2.2.6}$$

In equation (2.2.6), μ_t is called the eddy viscosity or the turbulence viscosity and depends on the flow unlike the molecular viscosity μ which is a property of the fluid. What makes the $k-\varepsilon$ model valid for the wall jet flow is the assumption about the Reynolds stresses made here. They are assumed to be proportional to the strain rate tensor, which is a valid hypothesis for simple flows such as straight boundary layers but which would be wrong in flows involving swirl, separation or strong accelerations. The two transport equations for respectively k and ε are given in (2.2.7) by

$$\begin{aligned}
&\frac{\partial}{\partial t}(\rho_0 k)+\frac{\partial}{\partial x_i}(\rho_0 k v_i)=\frac{\partial}{\partial x_j}\left[\left(\mu+\mu_t\right)\frac{\partial k}{\partial x_j}\right]+P_k-\rho_0\varepsilon \\
&\frac{\partial}{\partial t}(\rho_0 \varepsilon)+\frac{\partial}{\partial x_i}(\rho_0 \varepsilon v_i)=\frac{\partial}{\partial x_j}\left[\left(\mu+\mu_t\right)\frac{\partial \varepsilon}{\partial x_j}\right]+1.44\frac{\varepsilon}{k}P_k-1.92\rho_0\frac{\varepsilon^2}{k}
\end{aligned} \tag{2.2.7}$$

The turbulent viscosity is defined by $\mu_t = 0.09\rho_0 \frac{k^2}{\varepsilon}$ and the production of k is $P_k = -\rho_0 \langle v_i v_j \rangle \frac{\partial v_j}{\partial x_i}$.

We will now give more details about the specific parameters we used to solve our flow. The solver that was used to do so is the commercial code Ansys Fluent 12. As it has been indicated earlier in the text, the turbulence model chosen to solve this flow is the standard $k-\varepsilon$ with standard wall functions. The impact of this choice on the results will be discussed in the next section. We have in this problems three different types of boundary conditions associated to the boundaries of the domain. The edge on the left hand side of the settling chamber logically represents the inlet of the domain and was modeled as a velocity inlet. Figure 6 below shows the location of this boundary.

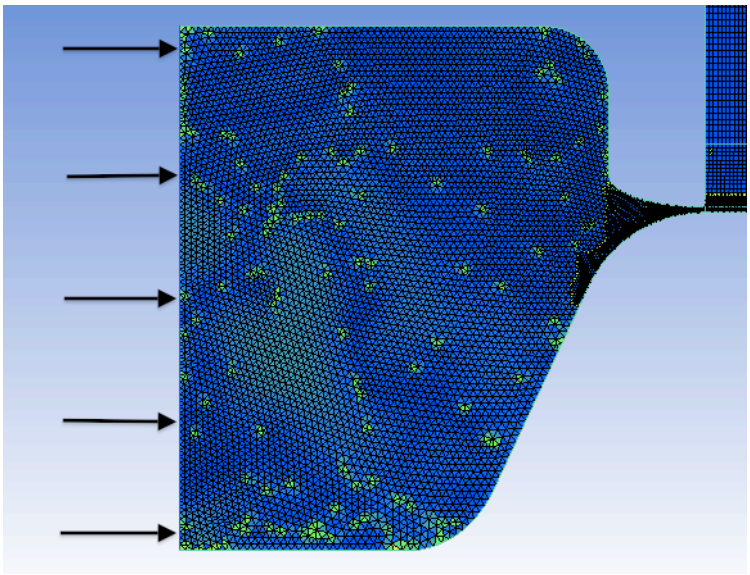

Figure 6: Inlet of the domain

The velocity to be specified at this boundary was calculated using the principle of conservation of mass applied between this inlet and the nozzle of the jet where we know

the nozzle velocity. Turbulence parameters also are to be specified at the inlet. We chose to indicate the turbulence intensity and the hydraulic diameter. The intensity was set at 4% and the hydraulic diameter is found to be equal to the length of the boundary (1247mm). The influence of these parameters on the solution will also be discussed in the following section. The second boundary condition to apply is to be at the outlet of the domain. The outlet could have been at different locations. However one made more sense than the others regarding the experimental set up. The outlet of the domain is a region that was created downstream the trailing edge of the test plate, slightly below its level. Figure 7 gives a close view of this region.

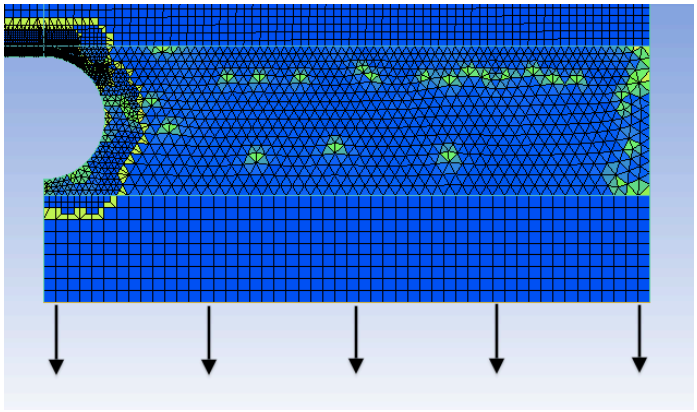

Figure 7: Outlet of the domain

The outlet was specified as a simple outflow. The advantage of this type of boundary condition is that no specific parameter is needed. The flow simply pours off the domain. All the other boundaries of the domain were set as walls. The discretization schemes for the pressure, the momentum, the turbulence kinetic energy and the turbulence dissipation rate were all of second order. The characteristics of the fluid are the Fluent standards for the air, a density of $1.225 kg/m^3$ and a dynamic viscosity of $1.7894.10^{-5} kg/ms$.

Therefore, the Reynolds number at the nozzle and for a jet velocity of $60m/s$ is $\mathrm{Re} = 52165$.

2.3. Results: RANS calculations of the flow

In this section we will detail some features of the solution. Several configurations were run with Fluent but we will focus on the one that worked best and discuss the influence of the different parameters of the model. We will consider a model with a velocity at the nozzle of $60m/s$. Figure 8 shows the velocity profile at the nozzle section.

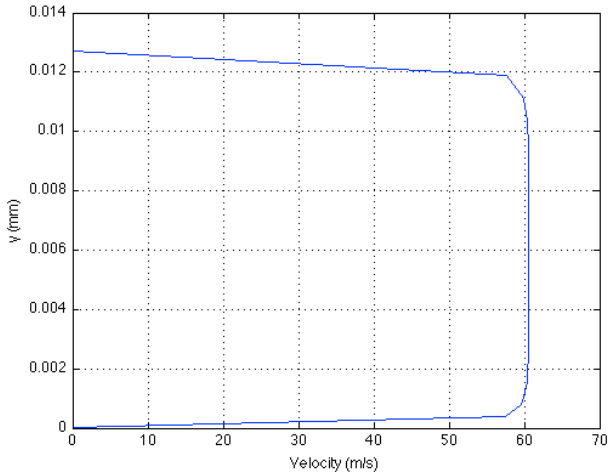

Figure 8: Velocity profile at the nozzle (x=0mm)

The most relevant graph in order to understand the flow inside the domain is certainly the representation of the pathlines colored by stream function showed in Figure 9.

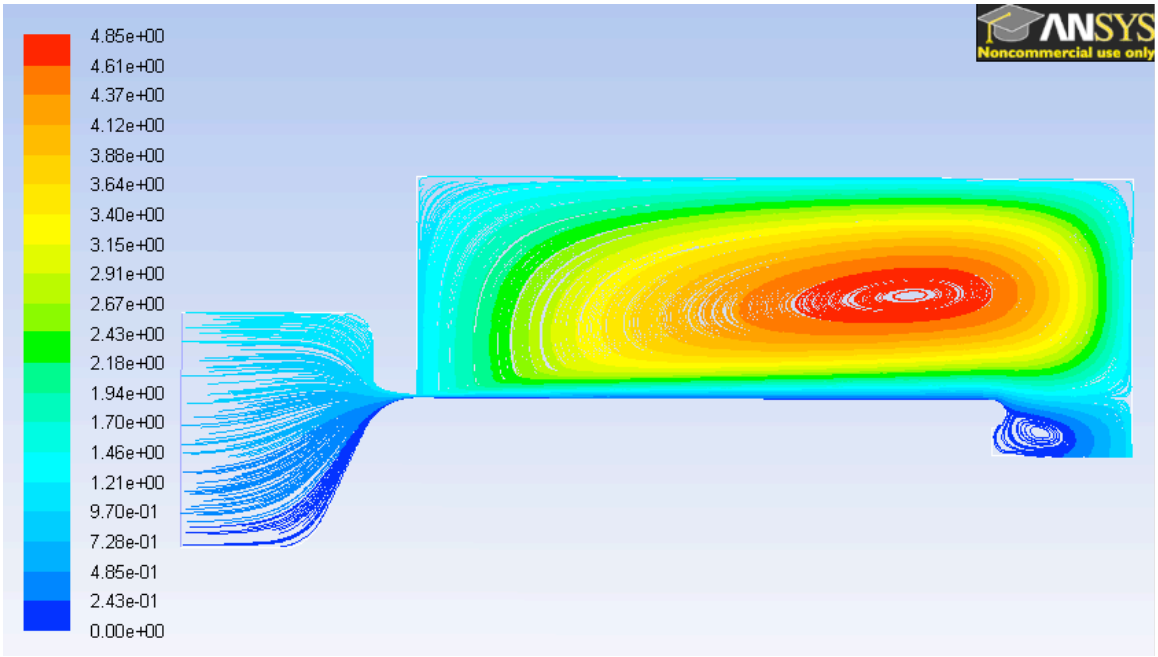

Figure 9: Pathlines colored by stream function (kg/s)

We clearly see with the help of this figure that a circulation of the flow is occurring within the tunnel. This pattern is probably induced by the wall jet itself.

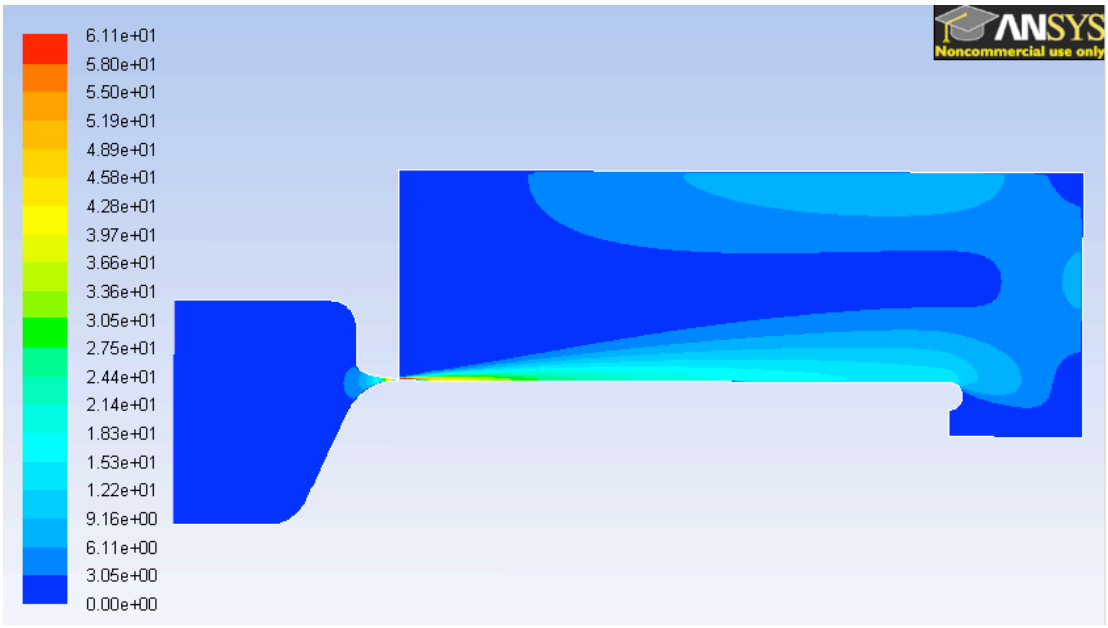

Figure 10: Contours of the velocity magnitude (m/s)

On Figure 10 we can observe the contours of the velocity magnitude and clearly identify the wall jet. Another interesting representation of the flow is the distribution of the turbulence kinetic energy showed in Figure 11. The main source of energy is obviously the straight nozzle of the jet as shown on Figure 12.

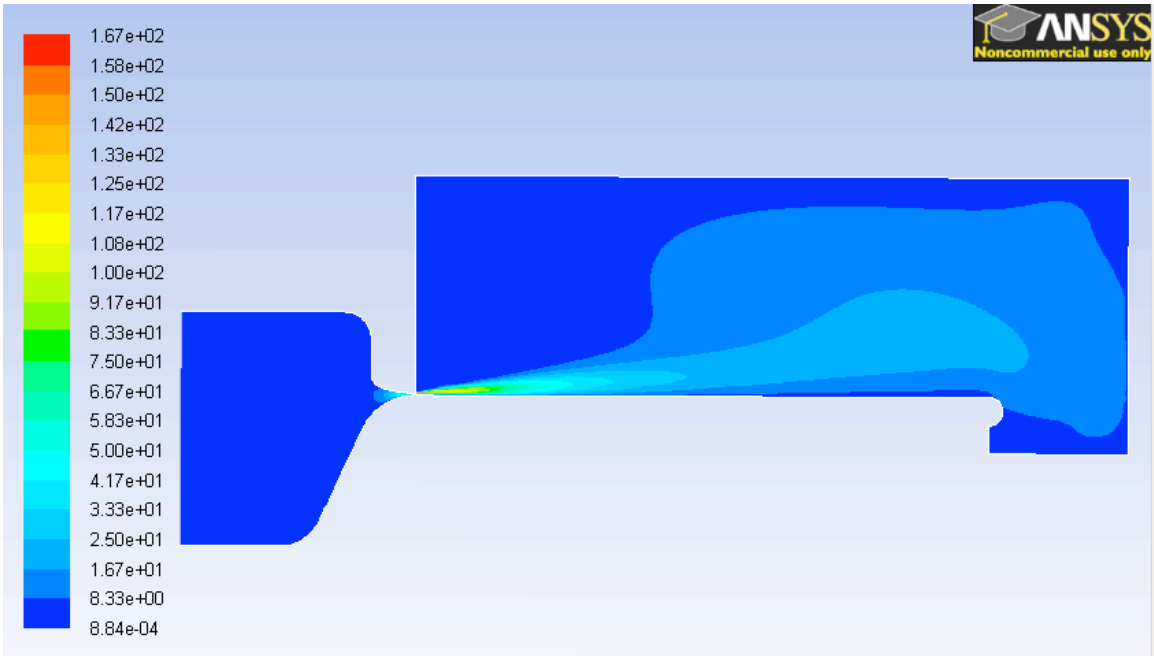

Figure 11: Contours of the turbulence kinetic energy (m^2/s^2)

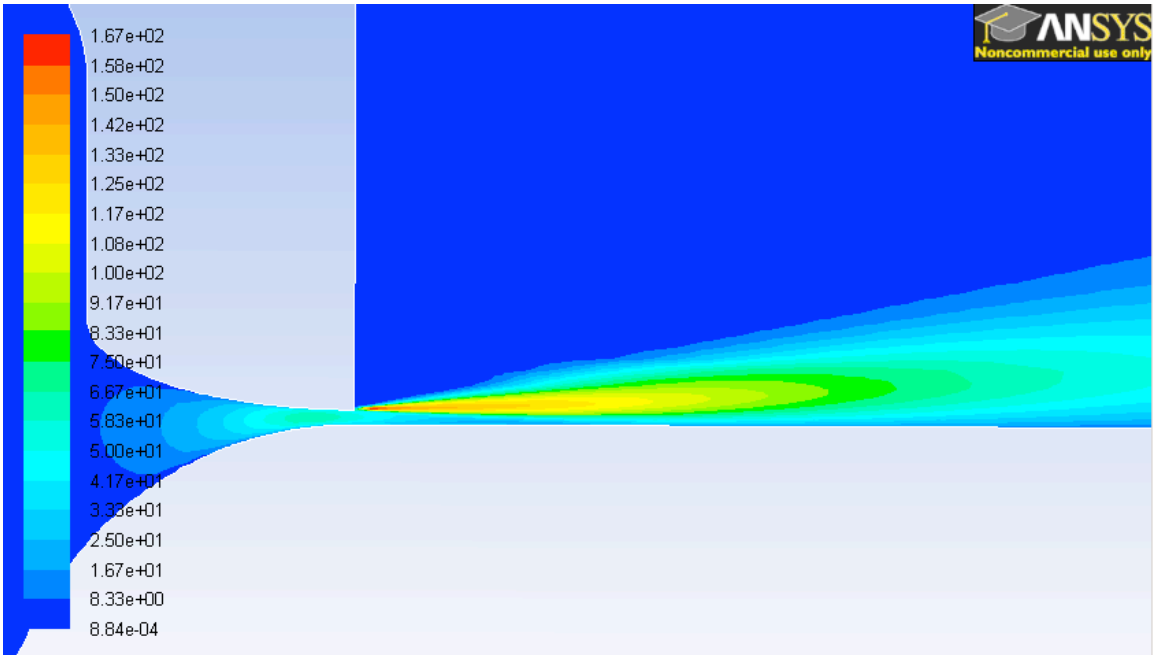

Figure 12: Contours of the turbulence kinetic energy (m^2/s^2) – zoom on the nozzle

The shape of the nozzle surprisingly has a critical impact on the solution. The first models to be run used to reproduce the exact geometry of the experimental set up. In other words, the upper lip of the nozzle was a semi-cylinder whose function was to smoothen the flow and reduce the production of turbulence kinetic energy. Most of the models that included this feature were divergent as represented on Figure 13.

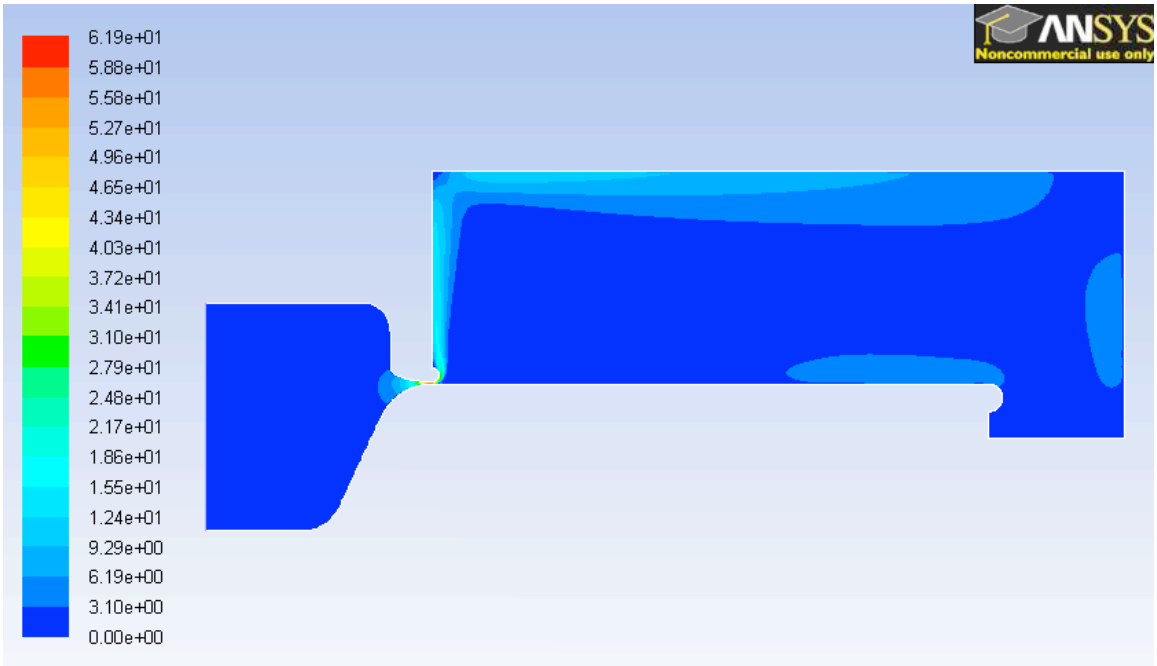

Figure 13: Contours of the velocity magnitude for a diverging model (m/s)

The flow is wrapping around this artifact of the nozzle and this initializes a clockwise circulation of the flow, in a non-physical fashion. Few models with a circular nozzle were convergent and showed an acceptable pattern of the flow. These models had to be run with a standard $k-\varepsilon$ model and second order discretization schemes. However, the resulting velocities were significantly lower than the velocities recorded in the experiments. Any other configuration including the circular shaped nozzle that was tested resulted in a diverging solution. It was then noticed that by forcing the flow to separate at the nozzle with the use of a sharp edge or, similarly, of a straight nozzle, the models that used to diverge were converging. This explains that this simpler geometry was adopted rather than one including the specifically designed nozzle. Also, the $k-\varepsilon$ turbulence model proved to give more accurate results than other models such as the $k-\omega$ model and so was chosen as the reference model. Finally, it is worth noticing that the turbulence

parameters set at the inlet boundary have little impact on the solution. The inlet turbulence is rapidly damped by the flow and most of the turbulence present in the wall jet is either self-generated by the flow itself or by the nozzle.

2.4. Results: comparison of the simulation to the experiments

After showing general aspects of the solution in the previous section, we will focus here on comparing the aerodynamic performances of the numerical simulation to the experimental values recorded at the facility in Virginia Tech. Figure 14 shows a comparison between the numerical and experimental velocity profiles at 1257mm downstream the exit of the nozzle. Figure 15 shows the same profiles but collapsed on the maximum velocity and on $y_{\frac{1}{2}}$ defined by $U\left(y_{\frac{1}{2}}\right)=\frac{U_{\max}}{2}$.

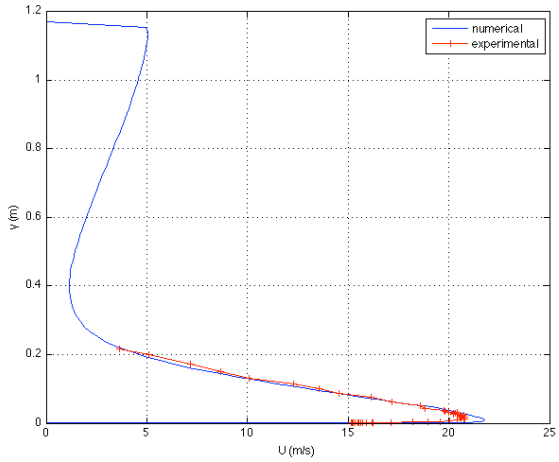

Figure 14: Numerical and experimental velocity profiles at 1257mm downstream the nozzle

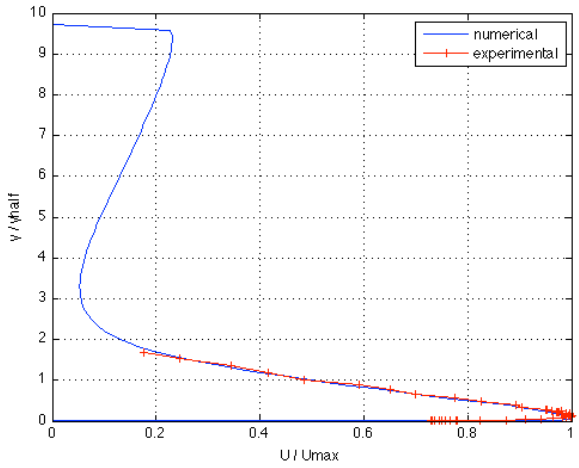

Figure 15: Collapsed velocity profiles at 1257mm

It is also worth looking at Figure 16 that zooms in the boundary layer region. From this plot we can evaluate the error between the numerical simulation and the experimental measurements. Based on the maximum velocity, we find an error lower than 5%.

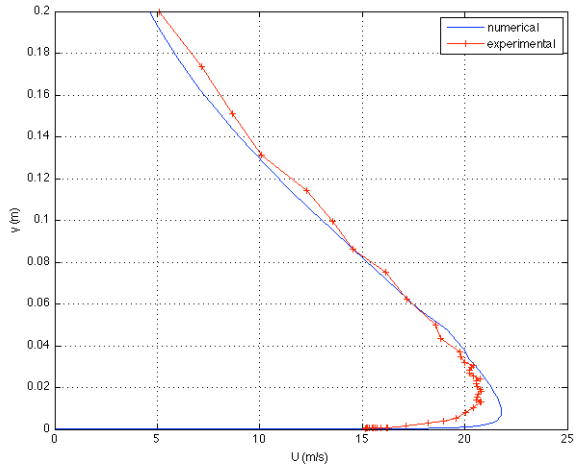

Figure 16: The boundary layer region

We adopt a slightly different approach for the turbulence kinetic energy. Measurements were available for v_1 only, the fluctuating velocity in the direction of the flow, while the

numerical simulation returned the distribution of the turbulence kinetic energy directly. The turbulence kinetic energy is defined by $k = \frac{1}{2}\left(v_1^2 + v_2^2 + v_3^2\right)$. In order to calculate the experimental turbulence kinetic energy, we need to make an assumption about the shape of the fluctuating velocities in the two other directions. It was found that $v_2^2 + v_3^2 = 2.5v_1^2$ gives a good fit as shown in Figure 17.

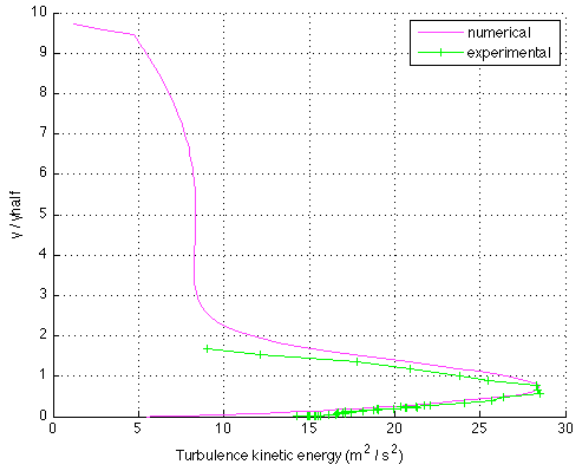

Figure 17: Numerical and experimental turbulence kinetic energy at 1257mm downstream the nozzle

The previous elements indicate that the numerical simulation that was performed is of good quality and is in good agreement with the experimental data. The numerical data thus being validated, we will use the distribution of the velocity, of the turbulence kinetic energy and of the turbulence dissipation rate in the next two chapters to compute the surface and far field pressure spectra.

CHAPTER 3: SURFACE PRESSURE SPECTRUM

3.1. Theory

The objective of this section is to show how the spatial distribution of the Turbulence Kinetic Energy in the boundary layer flow calculated numerically using a CFD model can be used to compute the spectrum of the pressure on the surface beneath the boundary layer.

This technique developed by Glegg *et al.* (2008) is based on the decomposition of the velocities in a boundary layer (or in any other two dimensional shear flow) into two components, the *w* component and the *s* component, which are orthogonal to each other. The *w* component has no velocity perturbation in the direction normal to the surface whereas the *s* component has no vorticity in this direction. It is also shown by solving the Poisson's equation for the pressure that the *w* mode does not cause any pressure fluctuation and that the *w* gust is convected with the local mean flow. It is therefore the *s* component that is responsible for the pressure fluctuations in the boundary layer and its vorticity is convected with the local mean flow.

3.1.1. Model for the velocity fluctuations in the flow

Glegg derived an analytical model for an unsteady flow in a two-dimensional boundary layer starting from the vorticity and continuity equations. He shows that the unsteady components of the velocity field in the wavenumber space and in terms of the function $u(\omega,k_1,k_3,x_2)$ are

$$\begin{aligned}
\hat{v}_1 &= -\frac{ik_1}{\lambda^2}\left(u' + \frac{k_3^2 U' u}{k_1^2 (U - U_0)}\right) \\
\hat{v}_2 &= u \\
\hat{v}_3 &= -\frac{ik_3}{\lambda^2}\left(u' - \frac{U' u}{(U - U_0)}\right)
\end{aligned} \tag{3.1.1}$$

In these equations we use a coordinate system (x_1,x_2,x_3) where x_1 is the direction of the flow and the boundary lies in $x_2=0$. k_i is the wavenumber in the *i-th* direction, v_i represents the velocity vector and U stands for $U(x_2)$ and denotes the mean flow. We also define $\lambda^2 = k_1^2 + k_3^2$ and $U_0 = -\frac{\omega}{k_1}$, ω being the frequency. The prime denotes a differentiation with respect to the direction normal to the boundary. Glegg showed that the function u is the solution to Raleigh's equation given in (3.1.2)

$$u'' - \left(\lambda^2 + \frac{U''}{(U - U_0)}\right)u = 0 \tag{3.1.2}$$

Equations (3.1.1) can be rearranged under the form

$$\hat{v}_i = \hat{s}_i + \frac{\hat{w}_i U'}{k_1 (U - U_0)} \tag{3.1.3}$$

with $\hat{s}_i = \left\{ -\frac{ik_1 u'}{\lambda^2}, u, -\frac{ik_3 u'}{\lambda^2} \right\}_i \quad \hat{w}_i = \left\{ -\frac{ik_3^2 u}{\lambda^2}, 0, \frac{ik_3 k_1 u}{\lambda^2} \right\}_i$

which introduces the *s* and *w* components cited previously. The two components are orthogonal, *s* has no vorticity in x_2 and *w* has no velocity in this same direction. The pressure fluctuation in the boundary layer can be found by solving the linearized form of Poisson's equation. The dependence will only be on the velocity perturbation in the x_2 direction, which shows that the *w* component does not participate in the pressure fluctuations.

3.1.2. Representation of the vorticity

Now that we have a model for the velocities in the flow, we want to introduce the vorticity. If we consider the vorticity of the *s* component of the velocity, we can obtain it by taking the curl of *s* and then eliminate the derivatives of *u* by using the fact that *u* satisfies Raleigh's equation given earlier in (3.1.2). We have been working in the wavenumber domain until now. The vorticity of *s* in the space/time domain is found by taking the inverse Fourier transform of the expression of the vorticity that was obtained following the previous description. The vorticty of *s* then takes the form:

$$\omega_j^{(s)}(x_i,t) = \int_0^\infty \int_{-\infty}^\infty \int_{-\infty}^\infty a_s(y_0,k_1,k_3)\delta(y_0 - x_2) e^{-ik_1(x_1 - U_0 t) - ik_3 x_3} \{k_3, 0, -k_1\}_j \frac{k_1}{\lambda^2} dk_1 dk_3 dy_0 \tag{3.1.4}$$

An important feature of the previous equation is the introduction of the function a_s defined by $a_s(y_0,k_1,k_3) = -2\pi\iota(-k_1U_0,k_1,k_3,y_0)U''(y_0)$, y_0 being the solution of $U_0 = U(y_0)$, the location above the wall at which $U = U_0$. With equation (3.1.4), we represent the vorticity of the *s*-component by a superposition of vortex sheets, the function a_s defining their strength, their amplitude. Note that *U''* representing the rate of change of shear in the flow, it will drop to zero outside the boundary layer, bringing the amplitude of the sheets of vorticity to zero in any region of the flow but within the boundary layer.

3.1.3. Relationship between velocity perturbations and a_s

The previous sections derived models for the velocity fluctuations and the vorticity within the boundary layer. The interest of using the vorticity was to bring up the notion of sheets of vorticity. Now we need to relate this concept to the velocity fluctuations. Glegg (2008) then introduced a vector potential ψ_j verifying $\nabla^2\psi_j = -\omega_j^{(s)}$. This equation can be solved assuming that the non-penetration condition is verified on the boundary and thus introducing an image source of vorticity below the wall. The previous reasoning suggests that the potential $\psi_j(x_i)$ could be defined as a superposition of vector potentials $\overline{\psi}_j(x_2,y_0,k_1,k_3)$ in a same fashion than in equation (3.1.4). Solving for the potentials $\overline{\psi}_j$ and taking the curl of it would give an expression of the *s* component of the velocity involving the amplitude of the vortex sheet strength a_s. A similar approach can be used for the *w* component of the velocity. Combining these two results in the expression of the

total velocity fluctuations in the boundary layer as a function of the amplitude of the vortex sheets (Glegg *et al.* (2008)).

$$v_j(x,t) = \int_0^\infty \int_{-\infty}^{\infty} \int_{-\infty}^{\infty} a_s(y_0,k_1,k_3)\left[\bar{s}_j(x_2,y_0,\lambda) + \bar{w}_j(k_1,k_3)\Gamma(y_0)\delta(x_2 - y_0)\right] e^{-ik_1(x_1 - U_0 t) - ik_3 x_3} dk_1 dk_3 dy_0$$

$$\text{with } \Gamma(y_0) = \frac{U'(y_0)}{U''(y_0)} \tag{3.1.5}$$

3.1.4. Introduction of the Turbulence Kinetic Energy

As it was discussed in chapter 2, CFD calculations using the RANS approach give information on the averaged values in the flow. Therefore we do not have any data concerning the fluctuating velocities involved in our development until this point. We cannot use our numerical results yet. However, the turbulence model we used provides us with information on the turbulence kinetic energy and turbulence dissipation rate distribution throughout the flow. Equations derived previously need to be related to this information.

The initial model for the velocity fluctuations in the flow was derived under certain assumptions. The flow we are interested in is a flow whose perturbations are homogeneous in the x_1 and x_3 directions of space and stationary in time. Therefore the quantity $u(\omega,k_1,k_3,x_2)$ is uncorrelated at different frequencies and wavenumbers. y_0 being a function of $\frac{\omega}{k_1}$, the function $a_s(y_0,k_1,k_3)$ should also be uncorrelated for different values of y_0 providing the mean flow is increasing monotonically with the distance above

the wall. This is not the case in our study; the flow admits a point of inflexion at the boundary layer thickness, it increases until that point and then decreases. So the flow is likely to have two points with different height above the wall but same velocity. However we will make the assumption that the sheets of vorticity are uncorrelated with the distance above the wall in this study. Consequently the wavenumber spectrum of the amplitude of the vortex sheets $S_{aa}(y_0,k_1,k_3)$ appears when writing the expected value of $a_s(y_0,k_1,k_3)$ under the relationship $E\left[a_s(y_0,k_1,k_3)a_s(y_0,k_1',k_3')\right] = R^{-1}S_{aa}(y_0,k_1,k_3)\delta(k_1-k_1')\delta(k_3-k_3')$. In this equation the parameter *R* denotes a non-dimensional lengthscale representative of the mixing length in the flow. Its exact value is still uncertain in the theory. Glegg (2008) defined it as the boundary layer thickness. We will consider alternative choices in this study. Using the expressions for the *s* and *w*-component of the total velocity separately, their contribution to the turbulence kinetic energy is given by:

$$q_s(x_2) = \frac{1}{2}E\left[|s_i|^2\right] = \int_0^R \int_{-\infty}^{\infty}\int_{-\infty}^{\infty} S_{aa}(y_0,k_1,k_3)\hat{q}_s(x_2,y_0,\lambda)\frac{k_1^2}{\lambda^2}dk_1dk_3dy_0 \qquad (3.1.6)$$

with

$$\hat{q}_s(x_2,y_0,\lambda) = \frac{1}{4}\left(e^{-2\lambda|x_2-y_0|} + e^{-2\lambda|x_2+y_0|} - 2H(x_2-y_0)e^{-2\lambda x_2}\right)$$

H(x) being the Heaviside function. Similarly, the contribution of the *w*-component to the turbulence kinetic energy is

$$q_w(x_2) = \frac{1}{2} E\left[|w_i|^2\right] = \frac{\Gamma(x_2)^2}{R} \int_{-\infty}^{\infty}\int_{-\infty}^{\infty} S_{aa}(x_2,k_1,k_3)\frac{k_3^2}{\lambda^2} dk_1 dk_3 \tag{3.1.7}$$

This yields the total turbulence kinetic energy $q = q_s + q_w$, the sum of the contributions from each of the two components of the velocity, as a function of the vortex sheet strength wavenumber spectrum.

3.1.5. Solving for the vortex sheet strength spectrum

We recall that the objective of this chapter is to develop the method permitting to obtain the surface pressure spectrum from RANS calculations of the flow. The pressure fluctuations are directly related to the velocity fluctuations by Poisson's equation. And the link between these velocity fluctuations and the turbulence kinetic energy that we know from our numerical simulations is the vortex sheet strength spectrum. This section shows how, for a known spatial distribution of the turbulence kinetic energy, we can obtain the vortex sheet strength spectrum S_{aa}. We will assume

$$S_{aa}(y_0,k_1,k_3) = A(y_0)E(\lambda L) \tag{3.1.8}$$

with

$$\int_0^{\infty} E(\lambda L)\lambda d\lambda = \frac{C}{L^2}$$

$A(y_0)$ is the unknown vortex sheet strength function we are looking for. $L(y_0)$ is the local turbulence lengthscale of the sheet, identical in both the streamwise and spanwise directions. Finally, the function $\lambda E(\lambda L)$ is the energy spectrum of the turbulence, assumed to be isotropic. C is a constant of the problem that will be calculated later. The *s* and *w*-component of the turbulence kinetic energy can be rewritten as follows

$$q_s(x_2) = \pi \int_0^R \int_0^\infty A(y_0)\hat{q}_s(x_2, y_0, \lambda) E(\lambda L) \lambda d\lambda dy_0 \tag{3.1.10}$$

$$q_w(x_2) = \frac{\pi \Gamma(x_2)^2}{R} A(x_2) \int_0^\infty E(\lambda L) \lambda d\lambda = \frac{\pi C \Gamma(x_2)^2}{RL^2} A(x_2) \tag{3.1.11}$$

Given this model, we can invert the relationships and use the known parameters of the flow (turbulence kinetic energy distribution, mean flow and local lengthscale) to find the unknown function $A(y_0)$ giving the vortex sheet strength spectrum.

3.1.6. Surface pressure spectrum

This last section aims at connecting every element together to directly relate what we want to what we know, the surface pressure spectrum to the turbulence kinetic energy distribution.

The first step towards the surface pressure spectrum is to derive an expression for the pressure fluctuations on the surface. An expression for the unsteady pressure can be given as a solution to the linearized Poisson's equation (Townsend, 1976). The expression for

the velocity fluctuations given in (3.1.3) is used in Poisson's equation, and with the help of Fourier transforms, we can express the pressure fluctuations in the flow and the pressure fluctuations on the surface if we consider the case $x_2 = 0$. This results in the following equation:

$$p_s(x_1,x_3,t) = \int_0^\infty \int_{-\infty}^\infty \int_{-\infty}^\infty a_s(y_0,k_1,k_3) P_e(y_0,\lambda) e^{-ik_1(x_1-U_0 t)-ik_3 x_3} \left(\frac{k_1}{\lambda}\right)^2 dk_1 dk_3 dy_0 \tag{3.1.12}$$

with

$$P_e(y_0,\lambda) = \int_0^\infty \left(e^{-\lambda|y-y_0|} - e^{-\lambda|y+y_0|}\right) U'(y) e^{-\lambda|y|} dy$$

The correlation function of the surface pressure fluctuations will involve this expression of $P_e(y_0,\lambda)$ along with the surface pressure wavenumber spectrum. The function $A(y_0)$ detailed in section 3.1.5 can be used to calculate the spectrum S_{aa}. With the help of the Fourier transform of this correlation function, we can write the expression of the wavenumber spectrum of the surface pressure, which, once integrated along the wavenumbers, give the power spectral density of the surface pressure fluctuations:

$$S_{PP}(\omega) = \frac{(\rho_0 U_\infty^2)^2 \delta_0}{U_\infty} \int_0^\infty \int_{-\infty}^\infty \frac{\omega^4 A(y_0)}{U_0^5 \lambda_0^4} \left|P_e(\lambda_0,y_0)\right|^2 E(\lambda_0 L) dk_3 dy_0 \tag{3.1.13}$$

U_∞ and δ_0 are the parameters used to scale velocities, distances, energies and frequencies all along the process in order to work in a dimensionless context. They appear here in order to switch back to the dimensional space.

3.2. Coding

3.2.1. Evaluation of the function $A(y_0)$

In this section we are going to show how we can achieve a numerical evaluation of the function $A(y_0)$ defining the vortex sheet strength spectrum through equation (3.1.10). We will start from the CFD data of the flow and work backwards to inverse the relationship relating the turbulence kinetic energy to A. Combining equations (3.1.10) and (3.1.11) we can define

$$q(x_2) = \int_0^R A(y_0)(Q_s(x_2, y_0) + Q_w(y_0)\delta(x_2 - y_0))dy_0 \tag{3.2.1}$$

with

$$Q_s(x_2, y_0) = \pi \int_0^\infty \hat{q}_s(x_2, y_0, \lambda) E(\lambda L)\lambda d\lambda$$

$$Q_w(y_0) = \frac{\pi C}{RL^2}\left(\frac{U'(y_0)}{U''(y_0)}\right)^2$$

If we combine the former definition of Q_s to the expression in equation (3.1.6) we can also write Q_s as

$$Q_s(x_2,y_0)=\frac{\pi}{4L^2}\left(F\left(\frac{|x_2-y_0|}{L}\right)+F\left(\frac{x_2+y_0}{L}\right)-2F\left(\frac{x_2}{L}\right)H(x_2-y_0)\right) \tag{3.2.2}$$

The function F being the Laplace transform of the energy spectrum $\lambda E(\lambda L)$ written as

$$F\left(\frac{x}{L}\right)=L^2\int_0^\infty e^{-2\lambda L\frac{x}{L}}E(\lambda L)\lambda d\lambda \tag{3.2.3}$$

A form for the energy spectrum was suggested by Glegg (2008) as

$$\xi E(\xi)=\xi^{-\frac{5}{3}}f_L(\xi)f_\eta(\xi) \tag{3.2.4}$$

$$f_\eta(\xi)=1$$

$$f_L(\xi)=\left\{1+\frac{c_R}{\xi^3}\right\}\left(\frac{\xi}{\left(1+\xi^2\right)^{\frac{1}{2}}}\right)^{\frac{17}{3}}$$

$$c_R=0.05$$

It should be noticed that there exist other forms of the function $f_L(\xi)$ such as $f_L(\xi)=\left(\frac{\xi}{\left(c_L+\xi^2\right)^{\frac{1}{2}}}\right)^{\frac{5}{3}+p}$, the constants c_L and p possibly taking different values as suggested by Pope (2000) or by the Von Karman spectrum. We can represent equation (3.2.1) in a numerical fashion as

$$q(m\Delta y) = A(n\Delta y)\left[Q_s(m\Delta y, n\Delta y)\Delta y + Q_w(m\Delta y)\delta_{mn}\right] \tag{3.2.5}$$

or

$$q_m = A_n\left[Q_{mn}\right]$$

giving

$$A_n = \left[Q_{mn}\right]^{-1} q_m \tag{3.2.6}$$

Hence we defined the function $A(y_0)$ we were looking for. The data necessary to compute this expression is known and can be obtained from the results of a CFD model of the flow.

a. Implementation of Q_w

Q_w is defined in equation (3.2.1) as $Q_w(y_0) = \frac{\pi C}{RL^2}\left(\frac{U'(y_0)}{U''(y_0)}\right)^2$. The value of R will be the object of an investigation in the final result. The mean velocity profile $U(y_0)$ at the point that we consider is readily available from the CFD data. *U'* and *U''* are computed from *U* using a first order finite difference scheme:

$$U_i' = \frac{U_{i+1} - U_i}{y_{i+1} - y_i}$$

$$U_i'' = \frac{U_{i+1}' - U_i'}{y_{i+1} - y_i} \qquad U_i = U(i\Delta y), \quad i = 1,...,N-1$$

In order to conserve a constant length for the numerical vectors, U_N', U_{N-1}'' *and* U_N'' were artificially set to the same value as the last defined point. The gradient of velocity being much smaller outside the jet than near the wall, this approximation is justified.

However, the evaluation of *U'* and *U"* is a problem near the wall. The velocity changes rapidly and shows large variations between two points a very small step away. Thus the profiles of *U'* and *U"* are uncertain in this region. This can be either an inherent characteristic of boundary layer flows or a lack of accuracy in the resolution of the CFD simulation near the boundary. Only further calculations with a much finer grid that would contain a considerably larger number of elements would shed light on this point. This issue with *U'* and *U"* affects the calculation of Q_w. Q_w being involved in the calculation of Q which is used in the calculation of A. This inaccuracy impacts much more than Q_w and can affect the final spectrum. This was addressed by experimenting a model for the ratio *U'/U"* until the point where *U'* and *U"* become acceptable. This model is given by Townsend (1978) for wall jets. He gives the velocity profile in the inner layer of a wall jet as $U = C_1\left[\ln\left(\frac{y}{C_2}\right) - \frac{y}{C_3}\right]$ which would result in a ratio $\frac{U'}{U''} = -y + \frac{y^2}{C_3}$ where C_3 is defined as the inner layer thickness (0.009m in the case of the study). Figure 18 shows a comparison between *U'/U"* calculated from the CFD values, its approximation detailed above and the profile resulting from the combination of the approximation until a certain point and the CFD values afterwards. Figure 19 gives the full profile that will be considered for *U'/U"* with the approximation to the lower values.

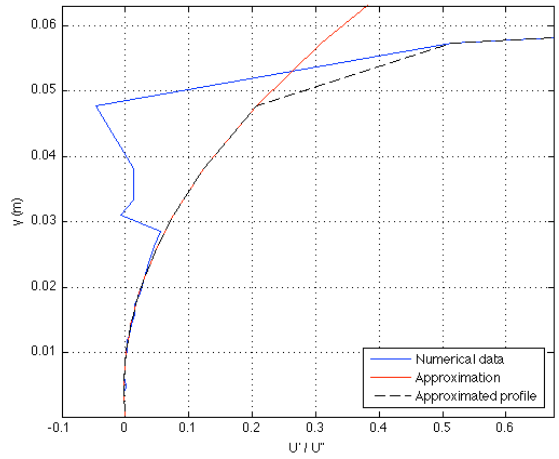

Figure 18: Approximation of *U'/U"* in the inner layer at 1352mm downstream the nozzle exit

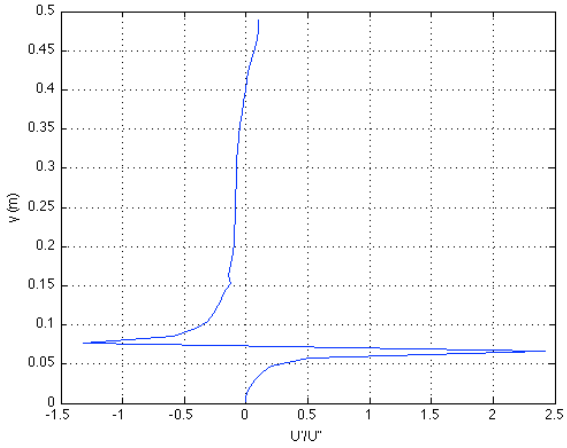

Figure 19: Approximated profile for U'/U"

Then the turbulence lengthscale is defined as $L = \alpha \frac{q^{\frac{3}{2}}}{2\varepsilon}$, q and ε being the turbulence kinetic energy profile and the turbulence dissipation profile respectively, available as RANS calculations outputs. L is a lengthscale representative of the turbulence in the flow and was shown by Townsend (1978) to be equal to y, the distance to the wall, in the region close to the wall. In other words, the slope of L plotted versus y must be 1 at the

wall. The constant α is a scaling constant to ensure that this slope is 1. Figure 20 shows the turbulence lengthscale profile and Figure 21 focuses on the boundary region where the slope is 1.

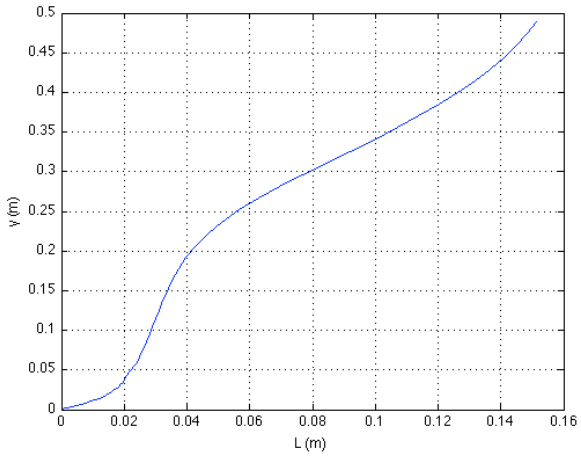

Figure 20: Turbulence lengthscale profile at 1352mm downstream the nozzle exit

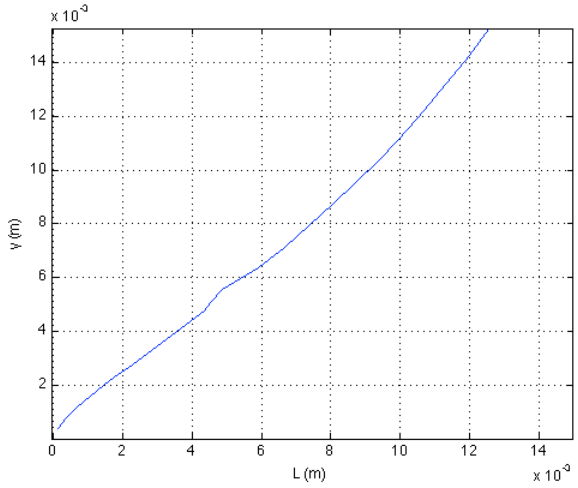

Figure 21: Boundary region of the turbulence lengthscale profile

We are left with the constant C to evaluate. It was defined in equation (3.1.8) as

$$\frac{C}{L^2} = \int_0^\infty E(\lambda L)\lambda d\lambda$$

$$\text{or } C = \int_0^\infty E(\xi)\xi d\xi \tag{3.2.7}$$

with the appropriate change of variable. Using the expression for the energy spectrum defined in (3.2.4), the integral to evaluate is finally

$$C = \int_0^\infty \xi^{-\frac{5}{3}} \left\{1 + \frac{0.05}{\xi^3}\right\} \left(\frac{\xi}{\left(1+\xi^2\right)^{\frac{1}{2}}} \right)^{\frac{17}{3}} d\xi \tag{3.2.8}$$

The former integral is carried out using the Matlab function *'quadgk'* which uses a Gauss-Kronrod quadrature (Calvetti *et al,* (2000)). The Gauss-Kronrod quadrature is a variant of the Gaussian quadrature. Instead of recalculating the abscissas of the points where to evaluate the integrand at each iteration until we reach an acceptable level of error, Kronrod (1964) showed how to pick the so-called *Kronrod points.* Using this set of points, abscissas of previous iterations can be reused as part of the current set of points. The result of this integration returns a value of C equal to 1.046. This allows us to complete the implementation of Q_w by using all these elements in equation (3.2.1).

b. Implementation of F

The evaluation of the function F defined by the relationship in equation (3.2.3) as

$$F\left(\frac{x}{L}\right) = L^2 \int_0^\infty e^{-2\lambda L \frac{x}{L}} E(\lambda L)\lambda d\lambda$$

$$\text{or } F(s) = \int_0^\infty e^{-\xi s} E(\xi)\xi d\xi \tag{3.2.9}$$

presents some issues to deal with. A numerical integration for $0 \le \xi < \infty$ requires a finite set of points spanning a range large enough to be considered reaching infinity and with a step fine enough to carry out a good evaluation of the integral.

One solution that was investigated is to split the integral over ξ into two parts. Thus we can carry out the integral numerically on $0 \le \xi \le K$ and take an approximation for $\xi >> 1$ on $K \le \xi < \infty$ that can be calculated analytically. This will reduce the number of points for ξ needed to carry out a numerical evaluation of the integral.

The integral between 0 and K is evaluated using the Matlab function *'trapz'* which implements a trapezoidal rule according to equation (3.2.10)

$$\int_a^b f(x)dx \approx \frac{b-a}{n}\left[\frac{f(a)+f(b)}{2} + \sum_{k=1}^{n-1} f\left(a + k\frac{b-a}{n}\right)\right] \tag{3.2.10}$$

The integrand $\xi E(\xi) = \xi^{-\frac{5}{3}}\left\{1 + \frac{c_R}{\xi^3}\right\}\left(\frac{\xi}{\left(1+\xi^2\right)^{\frac{1}{2}}}\right)^{\frac{17}{3}}$ admits an asymptotic value for $\xi >> 1$ as

$\xi E(\xi) \approx \xi^{-\frac{5}{3}}$. So the problem takes the form:

$$F(s) = \int_0^K e^{-\xi s} E(\xi)\xi d\xi + g(s) \tag{3.2.11}$$

with

$$g(s) = \int_K^\infty e^{-s\xi}\xi^{-\frac{5}{3}} d\xi \tag{3.2.12}$$

which is $g(s) = K^{-\frac{5}{3}}\frac{1}{s}e^{-s\xi}$ (3.2.13)

Figure 22 below shows the numerical evaluation of the function F as the sum of a numerical integration for $0 \le \xi \le K$ and of an approximation calculated analytically for $K \le \xi < \infty$. K was set to 10. For values of K greater than 10, we don't observe any changes in the final result which proves that K=10 is large enough to consider the approximation.

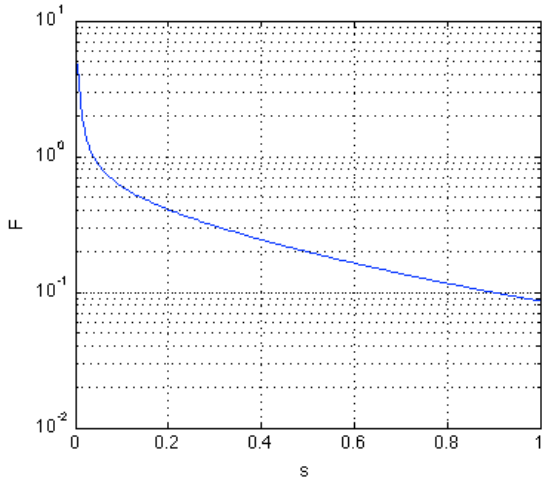

Figure 22: F evaluated using trapz between 0 and K and an analytical calculation of g

However this result is not completely accurate. If we look at the function *g* as defined in equation (3.2.13), we clearly see that it makes the final result to diverge when *s* tends to zero. Thus F is not defined at the singular point *s*=0 because of the contribution of *g*. As a matter of fact, at *s*=0 F should reduce to the integral of the energy spectrum defined in equation (3.2.9) and yield the constant C, which is finite and equal to 1.046.

Another approach consists in evaluating the function F using the Matlab function *'quadgk'* that was discussed earlier. This function can carry out the integration between 0 and infinity so we can get rid of that divergence problem at *s*=0 introduced by *g*. But the result of the integration is a function of the variable *s*, unlike the case where we were

evaluating the value of the constant C. So we need to numerically integrate for each value of the argument of F, which could result in a very time-consuming operation. Figure 23 below shows a comparison between F evaluated with the previous method employing the function *'trapz'* and this one using the function *'quadgk'*.

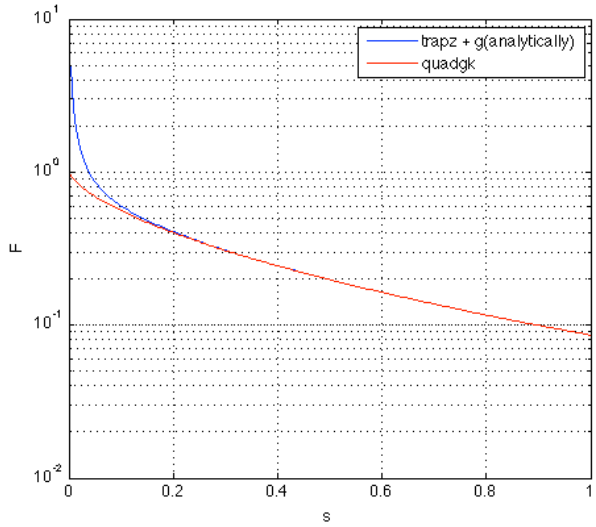

Figure 23: Comparison of evaluations of F using trapz and an analytical approximation of *g* in one hand and quadgk in the other hand

The plot shows a large difference using the function *'quadgk'* compared to the previous approach. The former converges to C exactly in s=0 and the latter diverges to infinity as we saw earlier. Moreover the function *'quadgk'* is finally less time-consuming and saves between 25% and 50% of the time necessary to carry out the integration for a given set of points of s. We also don't need to take any other approximation than the numerical one for this approach.

In order to make sure that this result is valid, we can also compare it to a third approach calculating g in a different manner. By using the change of variable $\xi = s^{-1}\gamma, d\xi = s^{-1}d\gamma$ in equation (3.2.12), we can write the function g as

$$g(s) = s^{\frac{2}{3}} \int_{sK}^{\infty} e^{-\gamma} \gamma^{-\frac{5}{3}} d\gamma \tag{3.2.13}$$

which is the incomplete gamma function

$$g(s) = s^{\frac{2}{3}} \Gamma\left(-\frac{2}{3}, sK\right) \tag{3.2.14}$$

The incomplete gamma function implemented in Matlab under the name *'gammainc'* does not accept a negative argument, so we carry out an integration by parts in (3.2.13) to yield the more convenient form:

$$g(s) = \frac{3}{2} s^{\frac{2}{3}} \left\{ e^{-sK} (sK)^{-\frac{2}{3}} + \Gamma\left(\frac{1}{3}, sK\right) \right\} \tag{3.2.15}$$

Figure 24 below shows (in red) F calculated with the function *'quadgk'* as detailed in the previous paragraph and also the implementation of the incomplete gamma function in equation (3.2.15) added to the previous evaluation of the integral for $0 \le \xi \le K$ using the trapezoidal rule (in black).

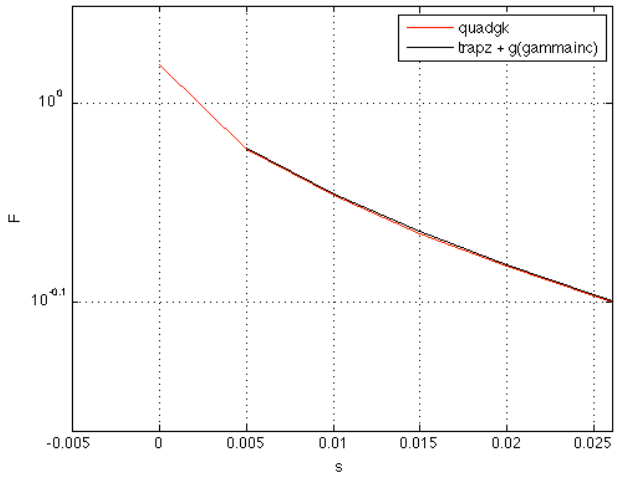

Figure 24: Comparison of evaluations of F using quadgk in one hand and trapz and an evaluation of *g* with gammainc in the other hand

We can observe that the two plots are in good agreement. However the gamma function solution returns an undefined value at s=0.

c. Implementation of Q_s

Q_s is defined in equation (3.2.2) by

$$Q_s(x_2,y_0)=\frac{\pi}{4L^2}\left(F\left(\frac{|x_2-y_0|}{L}\right)+F\left(\frac{x_2+y_0}{L}\right)-2F\left(\frac{x_2}{L}\right)H(x_2-y_0)\right)$$

This expression is implemented numerically by first calculating the arguments in each of the three functions F and then using an interpolation of F calculated in section *b.* at the specific points of interest. We chose the function F calculated with *'quadgk'* to compute the results, and we used the Matlab function *'interp1'* which implements a simple 1D interpolation of the data available. However a problem arises. The arguments in the three functions F involve the inverse of L and L can be very small in the boundary layer. Thus,

some of these arguments will be large and will span a wide range of values. F was calculated using a certain number of predefined points and this vector of values will have to include a very large number of points to span the full range of the arguments with a step small enough to carry out an accurate interpolation. This was the source of computational capabilities issues, so it was decided to use an approximation of F for the largest values of its argument *s*. F is defined by equation (3.2.9): $F(s) = \int_0^\infty e^{-\xi s} E(\xi)\xi d\xi$. $E(\xi)\xi$ can be developed under a polynomial form to yield $E(\xi)\xi = a + b\xi + c\xi^2 + ...$ If this expression is plugged into the integral defining F we obtain $F(s) = \int_0^\infty e^{-\xi s}(a + b\xi + c\xi^2 + ...)d\xi$ which represents a sum of Laplace transforms fairly straightforward to evaluate. F can be approximated as $F(s) = \frac{a}{s} + \frac{b}{s^2} + \frac{2c}{s^3} + ...$ Higher order terms can now be neglected with respect to the lower order ones if we consider large values of *s*. Considering that the coefficient *a* is 0 and that *b* is the constant c_R defined earlier, F reduces to $F(s) = \frac{c_R}{s^2}$ for large values of *s*. The matrix Q_s will be evaluated using two methods of calculating the function F; F will be computed with the numerical integration *'quadgk'* when its argument is too small to fit in the range where the approximation previously defined is accurate enough. If the argument is larger than a threshold value (set at *s=30*) then the approximation will be employed.

d. Implementation of *Q*

Q is defined by the relationship in (3.2.5), $Q_{mn} = Q_s(m\Delta y, n\Delta y)\Delta y + Q_w(m\Delta y)\delta_{mn}$. Therefore its implementation is relatively straightforward. As the step in y is not constant like in most of the cases where numerical data is used, we define a row vector $(\Delta y)_n = y_{n+1} - y_n$. $(\Delta y)_n$ cannot be defined this way for $n=N$ and is artificially defined to be equal to the case $n=N-1$. Hence the matrix Q_{mn} is calculated by multiplying each row of the matrix Q_s by the row vector $(\Delta y)_n$ element-by-element and then adding the vector Q_w on the diagonal.

e. Implementation of *A(y_0)*

The unknown vector A_n is straightforwardly defined by numerically inverting the former matrix Q_{mn} and multiplying it by the turbulence kinetic energy vector q_m. Figure 25 shows the profile of A.

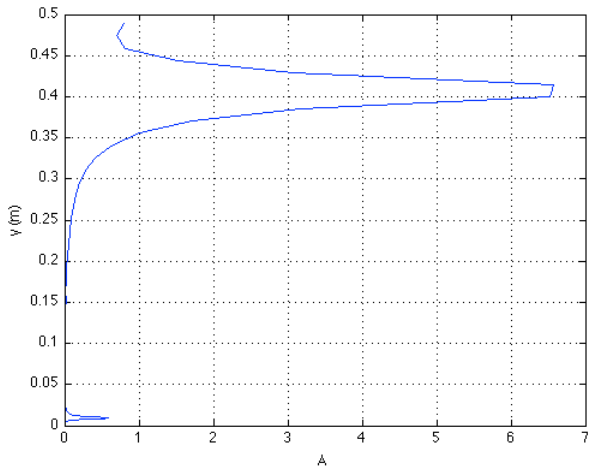

Figure 25: profile of A at 1352mm downstream the nozzle exit

This plot of the function A presents two peaks, the first slightly above the surface, at y=0.01m and the second much further away in the profile, outside the jet, at y=0.4m. These peaks are directly related to the profile of U'/U". Glancing back at Figure 18 and Figure 19, we see that U'/U" changes sign at three locations between y=0 and y=0.5m. Two of these locations correspond precisely to the locations of the two peaks in A. Where U'/U" changes of sign, it takes a very small value. This value makes Q_w to drop and affects also the matrix Q. When Q is inverted to calculate A, these two small values of Q result in large values of A. Concerning the third location where U'/U" changes of sign (y=0.07m on Figure 19) things are different. U'/U" changes sign but not slowly as for the two other points. It quickly goes from a relatively large positive value to a large negative value. When U'/U" is squared to obtain Q_w this results in a large positive peak, unlike the two other points which result in very small values. Therefore the effect of this third point on A is opposite to the two former ones. Whereas they created peaks in A, this one creates a drop. Figure 26 clearly illustrates that. We see two low values where U'/U" changes of sign smoothly and one large value where U'/U" changes of sign discontinuously. Figure 27 shows A also, but on a different scale. It highlights that peaks and drops in Q_w correspond to drops and peaks respectively in A.

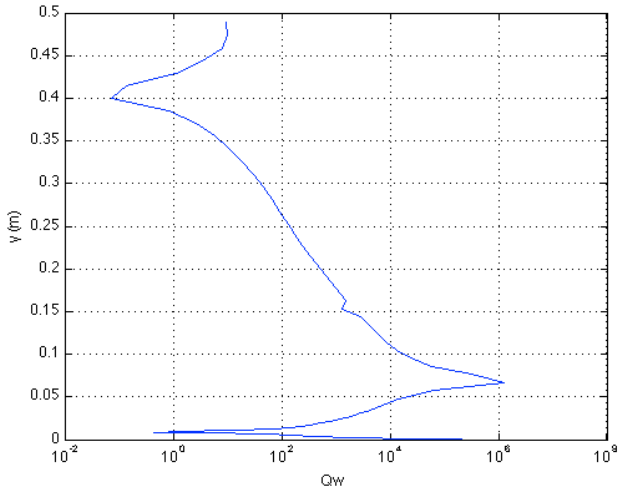

Figure 26: profile of Qw

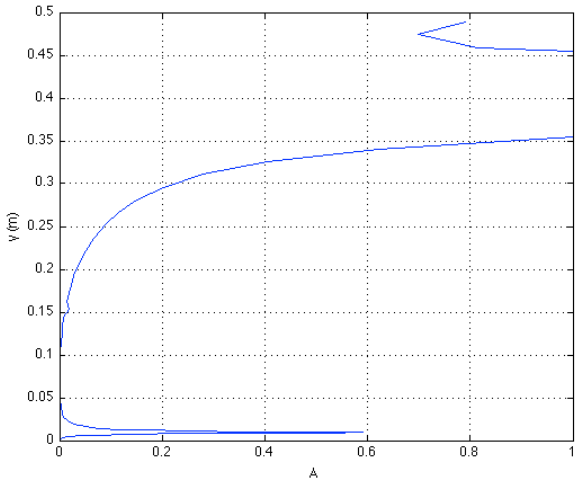

Figure 27: profile of A at 1352mm downstream the nozzle exit

The conclusion here is that A is highly dependant on U'/U". This justifies the choice of taking an approximated profile of U'/U" for the lower values and strengthen the point that a more accurate simulation of the flow could be useful. It is also noteworthy that the value of A is determined by the minimum of Q_w and this could lead to useful approximate or scaling results in the future.

3.2.2. Evaluation of the surface pressure spectrum

The function $A(y_0)$ can be used to compute the surface pressure spectrum given in equation (3.1.13). However, it appeared that this form was not suitable for a numerical evaluation. Also Glegg derived an approximation of the surface pressure spectrum given in equation (3.2.16) where the integral over k_3 is approximated. The spectrum becomes

$$S_{pp}(\omega) \approx \frac{\left(\rho_0 U_\infty^2\right)^2 \delta_0}{U_\infty} \int_0^\infty \frac{\pi\omega}{2} \frac{A(y_0)}{U_0^2} \left| P_e\left(y_0, \frac{\omega}{U_0}\right) \right|^2 E\left(\frac{\omega L}{U_0}\right) dy_0 \tag{3.2.16}$$

The function P_e was defined in (3.1.12) by the relationship

$$P_e(y_0, \lambda) = \int_0^\infty \left(e^{-\lambda|y-y_0|} - e^{-\lambda|y+y_0|} \right) U'(y) e^{-\lambda|y|} dy$$

This definition of P_e involves the integration of the derivative of U. Given the boundary layer shape of the velocity profile, its derivative admits huge gradients in the very few points close to the surface. This is not a suitable function to integrate numerically. Therefore we perform an integration by parts to reduce the order of U. P_e then takes the more convenient form

$$P_e(y_0, \lambda) = 2\int_{y_0}^\infty U(y) \lambda e^{-\lambda(2y-y_0)} dy - 2\int_0^\infty U(y) \lambda e^{-\lambda(2y+y_0)} dy \tag{3.2.17}$$

Also, the surface pressure spectrum requires $P_e\left(y_0, \frac{\omega}{U_0}\right)$. Equation (3.2.17) needs to be evaluated for $\lambda = \frac{\omega}{U_0}$, ω being a vector of arbitrary values of angular frequencies spanning the frequency range 200Hz-20kHz and defined numerically to build the final pressure spectrum. The integrals in equation (3.2.17) are carried out using the trapezoidal rule *'trapz'*. The method used to deal with the two output variables y_0 and λ was to compute the integral for each y_0 and assuming y_0 to be a constant in each step. Equation (3.2.16) can now be evaluated. ρ_0 is the density of the fluid, U_∞ and δ_0 are set to 1 as dimensions were conserved in this study. The integral is also carried out with a trapezoidal rule, the most convenient way to evaluate integrals whose integrands are numerical data instead of defined functions.

3.3. Results

We use experimental data made available by Alexander (2009) as a reference to compare the results returned by this simulation. We will focus on a case where the nozzle velocity is 60m/s and where the surface pressure spectrum is measured and calculated at a location 1352mm downstream the nozzle exit. Figure 28 shows the surface pressure spectrum obtained for different values of the parameter R involved in the definition of Q_w.

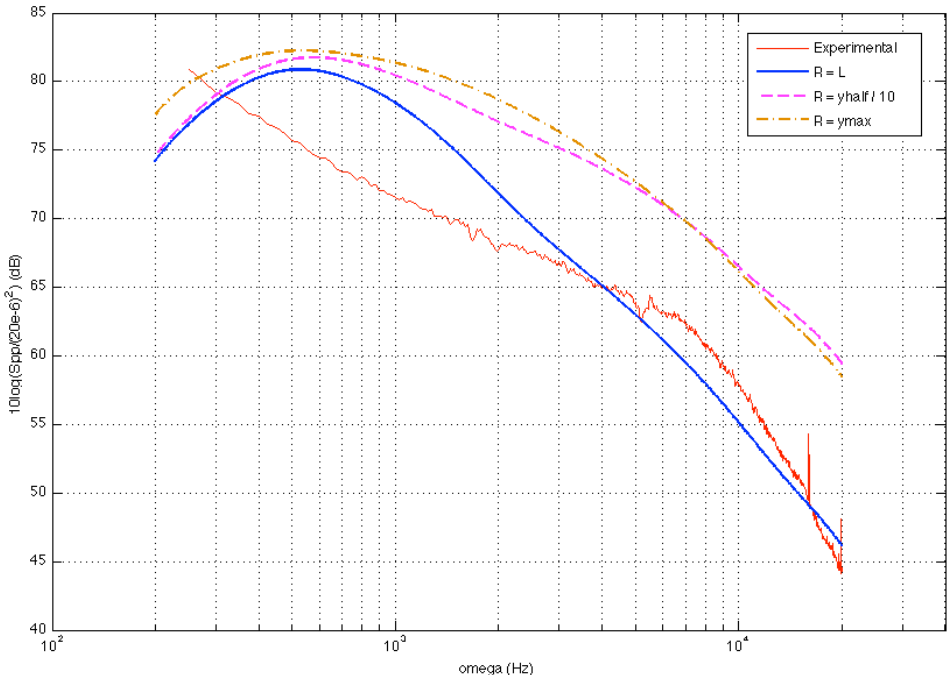

Figure 28: Surface pressure spectra at 1352mm downstream the nozzle for different values of the parameter R

R was chosen to be equal to two different constants, $\frac{y_{1/2}}{10}$ and $y_{\max}$ (having a factor of about 40 from one to another) and to the lengthscale which varies along with distance from the wall. From Figure 28, the case $R = L$ appears to give a good fit in level and the slope for the spectrum at high frequency matches the experiments best. This aspect is the most significant in the comparison of the results because the experimental data are affected by noise at low frequencies. The difference in the level is about 3dB in the high frequencies for the case $R = L$ and about 15dB for the two other cases.

Lets now look at the spectrum obtained with the approximation of U'/U", in the case that seems to be the most satisfactory, $R = L$.

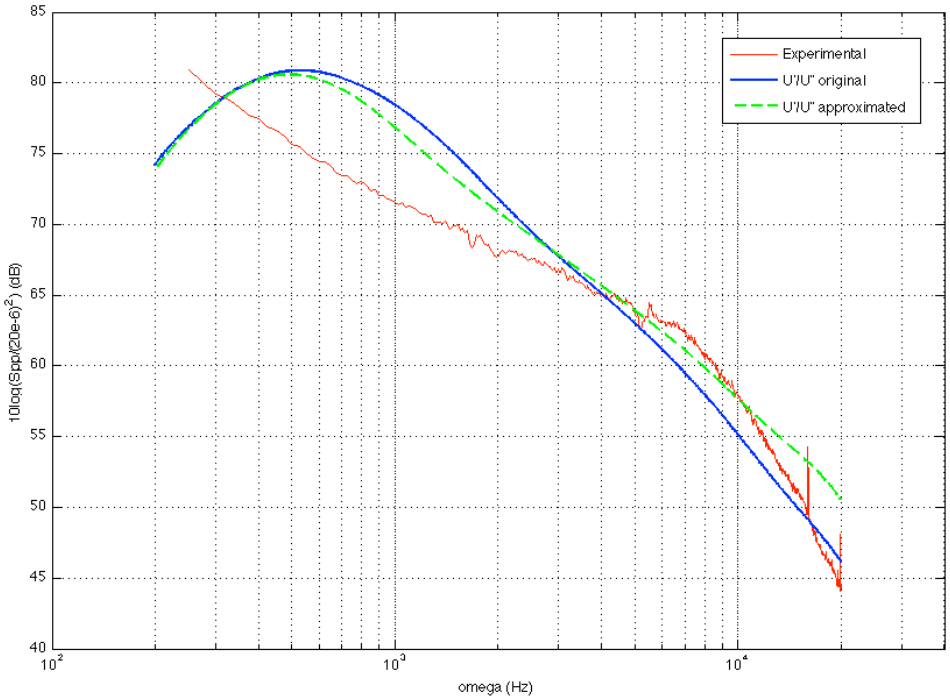

Figure 29: Surface pressure spectra at 1352mm downstream the nozzle with and without the approximated profile of U'/U"

Figure 29 shows that the approximation of U'/U" has some impact at high frequency and result in a 4dB difference at 20kHz. It is tempting not to consider it in order to stay closer to the experiments at high frequency and conserve a steeper slope that would also be more similar with the measured spectrum. However, as the approximation clearly removes noise from the profile of U'/U", we can infer that the dashed spectrum is a more accurate result of the simulation than the solid one although the fit to the experiments in the former case is not as good as in the latter. We could gain some insight into this point with further CFD studies improving the resolution of the grid and the profile of U'/U" thus.

It must be specified that all vectors of data have their first point located not at y=0m but at y=0.0004m, the location of the closest point to the wall. Although the CFD simulation returned data for the case y=0m, this point can cause errors in the context of this theory. As it can be seen in equations 3.2.1, 3.2.2 or 3.2.17 that involve 1/L or 1/U, a value of 0 for L or U at y=0m would result in a singularity in these equations.

Lastly, a factor of $10\log(4\pi) = 11dB$ was added to all the calculated spectra shown in the figures above. The expression for the near field spectrum that was derived in this theory can be used to calculate the r.m.s pressure as $p_{rms}^2 = \int_{-\infty}^{+\infty} S_{pp}(\omega)d\omega$. We can reach the same result using the spectrum that was measured with $p_{rms}^2 = \int_{0}^{+\infty} G_{pp}(f)df$. Given that $S_{pp}(\omega) = S_{pp}(-\omega)$ and that $\omega = 2\pi f$, we find that $G_{pp}(f) = 4\pi * S_{pp}(f)$. In order to represent the same quantity than what was measured in the experiments, it is necessary to multiply $S_{pp}(\omega)$ that was calculated numerically in this chapter by a factor of 4π.

CHAPTER 4: FAR FIELD PRESSURE SPECTRUM

4.1. Theory

The objective of this section is to give some insight into roughness noise. Its nature and its origin will be introduced in this chapter. We will develop a theory by Glegg and Devenport (2009) establishing a relationship between the surface pressure spectrum and the far field acoustic spectrum, providing some assumptions are made about the flow.

Rough surfaces are much noisier than smooth ones. Cole (1980) was the first to perform a study of the roughness noise in a wind tunnel. His work showed that there is a difference of approximately 3 dB between a flow over a smooth and over a rough surface. Liu *et al.* (2006) also studied a theoretical model describing the scattering of the turbulence near field into sound by roughness elements. It was shown that the roughness height and roughness density have a significant impact on the far field radiated noise, the roughness height having a dominant effect. We can identify three different effects of roughness elements on a flow as shown on Figure 30. The first is to enhance the existing turbulence in the boundary layer, the second is to increase the skin friction which appears as vortices in the wake of the roughness elements and the last one is to scatter propagating or convected pressure waves in several directions. It was shown by Lighthill (1952) that turbulence in a free stream flow creates a sound radiation of quadrupole

order. Then if we consider a turbulent flow over a smooth surface, we can assume that the surface behaves as a simple passive reflector providing a few conditions such as the acoustic wavelength to be large compared to the boundary layer thickness and the fluctuating shear stress to be neglected (Howe 1984). Hence, a turbulent flow is not influenced by the presence of a smooth surface and the radiated sound field still scales as a quadrupole. The change induced by a rough wall comes from the unsteady component of the skin friction and from the scattered field by roughness elements that both behave as dipole sources (Curle 1955). Given that the acoustic intensity of a dipole scales as $\rho_0 U^3 M^3$ and that the intensity of a quadrupole does as $\rho_0 U^3 M^5$, ρ_0 being the flow density, U the flow speed and M the Mach number, there will be an order of $\frac{1}{M^2}$ when switching from a smooth surface to a rough surface. This explains that for low subsonic flows (M<<1), a boundary layer over a rough surface radiates sound significantly more efficiently than a boundary layer over a smooth wall or in a free stream.

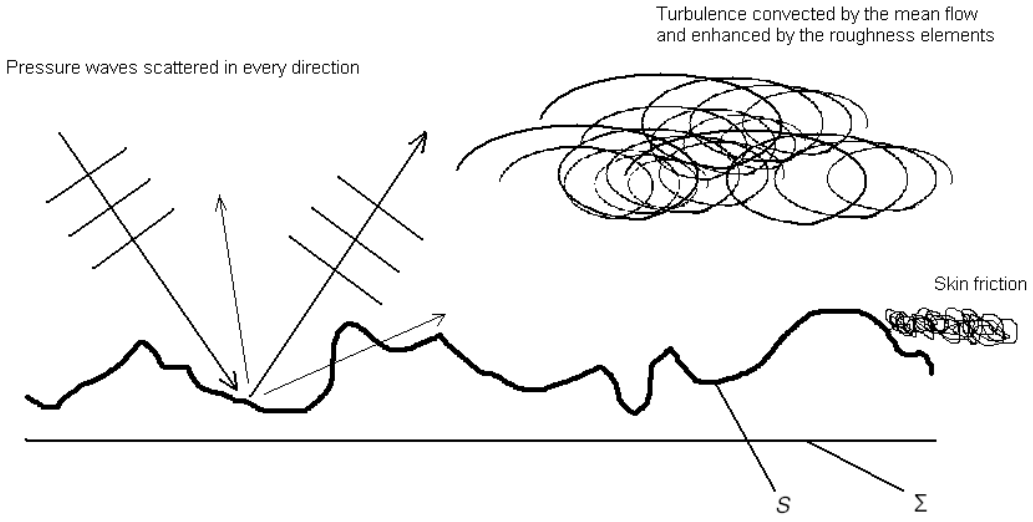

Figure 30: Mechanisms of sound generation within the turbulent boundary layer over a rough wall

The starting point of the theory derived by Glegg and Devenport (2009) is the well-known acoustic analogy developed by Lighthill (1952) and widely used to solve the acoustic far field in aero or hydroacoustics problems. We will use the solution to Lighthill's equation given by Goldstein (1976) in (4.1.1)

$$\rho(x,t)c_\infty^2 = -\int_{-T}^{T}\int_S \rho_0 V_n \frac{\partial G}{\partial \tau} dS(y)d\tau + \int_{-T}^{T}\int_S f_i \frac{\partial G}{\partial y_i} dS(y)d\tau + \int_{-T}^{T}\int_V T_{ij}(y,\tau)\frac{\partial^2 G}{\partial y_i \partial y_j} dV(y)d\tau \tag{4.1.1}$$

This equation represents the pressure perturbation $p(x,t) = \rho(x,t)c_\infty^2$ generated by a boundary layer turbulent flow in the region V bounded by surfaces S. The first integral on the left involving the velocity normal to the surface V_n can be eliminated if we consider a rigid surface. The two other terms involve the Green function G, solution to the wave equation. The second term in the middle shows a single derivative of G indicating a dipole source whereas the term on the right-hand side features a second derivative of G, representing a quadrupole source. Following the previous reasoning showing that in a low Mach number flow featuring both dipole and quadrupole source terms, the far field radiation will be induced by dipole sources only, we can make the assumption of ignoring the quadrupole source term with regard to the dipole source term. Under these assumptions, equation (4.1.1) reduces to

$$\rho(x,t)c_\infty^2 = \int_{-T}^{T}\int_S f_i \frac{\partial G}{\partial y_i} dS(y)d\tau \tag{4.1.2}$$

where f_i represent the forces per unit area applied by the surface S on the fluid. We can write these forces under the more practical form $f_i = p_S n_i - S_{ij} n_j$ where p_S is the unsteady component of the pressure on the surface, n_i represents the unit vector normal to the surface S in the *i-th* direction and into the volume V and S_{ij} is the viscous stress tensor. What we want to obtain is the former expression of the pressure fluctuations in the far field as a function of the pressure fluctuations on the surface and of the surface roughness characteristics, two elements known in our study. Therefore we start by defining a frame (y_1, y_2, y_3) where the flow is in the y_1 direction and the rough surface lies on the y_1, y_3 plane. The rough surface can then be defined by the function ξ so that $y_2 = \xi(y_1, y_3)$. The Green function in equation (4.1.2) is chosen to be the free field Green function. This Green function must account for the boundary conditions, i.e. a non-penetration condition on the surface $y_2 = 0$. With this intent, an image source is introduced below the surface at an equal distance of the surface than the source.

Equation (4.1.2) requires the divergence of G on the surface $y_2 = \xi$. This is obtained by using a Taylor series expansion of the gradient of G on the actual surface ξ, providing that the roughness height or the surface displacement is small compared to the acoustic wavelength. This hypothesis also allows us to consider the leading order terms only in this expansion. By using the proper expression of the Green function defined previously and involving Dirac delta functions, the gradients of G can be expressed on the actual rough surface using derivatives of the Dirac delta function. Once the derivatives of G are defined, they can be introduced in equation (4.1.2). In the process, the derivatives of the Dirac delta functions appearing in the divergence of G can be transferred to the forces f_i,

thus defining a retarded time, representative of the lapse in time existing between the emitting time and the receiving time. The forces applied by the surface on the fluid are constituted by the shear stresses and by the pressure. In the hypothesis where we neglect the shear stress tensor in the boundary layer, the forces exerted by the surface on the fluid reduce to the unsteady surface pressure only. Equation (4.1.2) becomes a function of the derivatives of the surface pressure with respect to space directions. Also, the integral in equation (4.1.2) would be carried out more easily on the projected plane Σ of the rough surface rather than on the actual rough surface *S.* This is achieved by expressing the unit vectors n_i normal to the surface as a function of the gradients of ξ. The frequency spectrum of the surface pressure appears by taking a Fourier transform with respect to time of the surface pressure fluctuations and of its derivatives. This integral over time will also take the retarded time into account in the exponential of the Fourier transform. All these operations result in the following expression of the pressure fluctuations in the far field of a turbulent boundary layer over a rough wall, in the frequency domain:

$$\rho(x,\omega)c_\infty^2 \approx -\frac{ik_0 e^{ik_0|x|}}{2\pi|x|}\int_\Sigma \left\{\left(\frac{x_1}{|x|}\frac{d\xi}{dy_1}+\frac{x_3}{|x|}\frac{d\xi}{dy_3}\right)-\frac{ik_0\xi x_2^2}{|x|^2}\right\}p_S(y,\omega)e^{-ik_0\frac{x_1y_1+x_3y_3}{|x|}}d\Sigma(y) \qquad (4.1.3)$$

We notice that $|x|$ represents the distance between the source and the observer, x_i here being the distance in a single direction. The wavenumber is defined by $k_0 = \frac{\omega}{c_\infty}$. This equation is written as an approximated value due to the approximation considered in the Taylor series expansion. Also, each term is dependent upon the roughness height ξ.

Therefore, if we consider a smooth surface where $\xi = 0$, equation (4.1.3) drops to zero and predicts an absence of noise in the far field. This actually means that the acoustic far field will be of quadrupole order and will be generated by the terms that we neglected earlier with respect to the roughness dipole terms.

4.2. Coding

In the previous paragraph, we succeeded in giving an equation relating the pressure perturbation in the far field to the pressure fluctuations on the rough surface beneath the boundary layer, in the frequency domain. However, the result still includes an integral over the planform and is not convenient for a numerical implementation. In this paragraph we will show how Glegg and Devenport could modify and simplify equation (4.1.3).

The first step is to switch to the wavenumber domain. Therefore, they take the wavenumber transform of equation (4.1.3) to express the surface pressure not only in the frequency but also in the wavenumber domain. Moreover, they define the wavenumber transforms ζ of the surface roughness ξ and of its gradients $\frac{\partial \xi}{\partial y_i}$. Equation (4.1.3) becomes

$$\rho(x,\omega)c_\infty^2 \approx -\frac{ik_0 e^{ik_0|x|}}{2\pi|x|}\int_k p_S(k_1,k_3,\omega)\left\{\left(\frac{x_1\zeta^{(1)}}{|x|}+\frac{x_3\zeta^{(3)}}{|x|}\right)-\frac{ik_0 h\zeta^{(2)}x_2^2}{|x|^2}\right\}(2\pi)^2 dk_1 dk_3 \qquad (4.2.1)$$

This equation gives the frequency spectrum of the pressure fluctuations at a specific location in the far field. It still features an integral, but which is carried out on the wavenumbers. After assuming that the surface pressure perturbations are homogeneous over the planform, an assumption that was already made in the chapter 3 as a justification for the uncorrelation of the vortex sheets, we can use the former expression of the far field pressure fluctuations to give their power spectral density using their expected value.

$$\Phi_{pp}(x,\omega) = \frac{\pi}{T} E\left[\left|\rho(x,\omega)c_{\infty}^{2}\right|^{2}\right] \tag{4.2.2}$$

This is the quantity that is to be used to quantify, analyze and compare the noise radiated at the far field by our flow. However it still needs to be directly related to the only information we know, $S_{pp}(\omega)$, the power spectral density of the pressure fluctuations on the surface.

Glegg and Devenport define the wavenumber spectrum of the surface pressure $S_{pp}(k_1,k_3,\omega)$ by the expected value of the product of the surface pressure wavenumber transform and its conjugate. It naturally appears in the expression we obtain when combining (4.2.1) and (4.2.2). Using the fact that the power spectral density of the surface pressure $S_{pp}(\omega)$ can be written as the integral of its wavenumber spectrum along the wavenumbers, $S_{pp}(\omega)$ arises from equation (4.2.2). Also, they arrange the resulting expression of $\Phi_{pp}(x,\omega)$ so that it is the integral of the product of a normalized surface pressure wavenumber spectrum $\Psi_{PP}(k_1,k_3,\omega) = \frac{S_{pp}(k_1,k_3,\omega)}{S_{pp}(\omega)}$ with a wavenumber filter

$\Theta(k_1,k_3,k_0)$ taking into account the wavenumber transforms of the surface roughness in the three directions of space. The normalized wavenumber spectrum Ψ_{PP} is a strongly dependent on the flow in the boundary layer. It represents the source terms and it will be highly influenced by the flow characteristics or the height of the roughness elements. Θ, however, is only driven by the geometrical characteristics of the rough wall and can be evaluated providing the roughness details are known. This function is independent of the flow and acts as a filter on the normalized surface pressure wavenumber spectrum Ψ_{PP} to adapt to each case of rough surface. The expression for the power spectral density of the far field pressure is given in the form

$$\Phi_{pp}(x,\omega) \approx \frac{4\pi^2 (k_0 h)^2 \Sigma S_{pp}(\omega)}{|x|^2} \int_{\kappa} \Psi_{PP}(k_1,k_3,\omega)\Theta(k_1,k_3,k_0)dk_1 dk_3 \qquad (4.2.3)$$

The last task is to find a method to evaluate the integral of the two formerly defined functions Ψ_{PP} and Θ. In this perspective, we will consider for our study the case of a rough surface constituted of N randomly distributed roughness elements with almost vertical sides, located at $\left(y_1^{(n)},y_3^{(n)}\right)$. The area beneath each roughness element is defined by $d\Sigma^{(n)} = \Delta y_1^{(n)} \Delta y_3^{(n)}$ and their roughness slope by $\left(\frac{\partial \xi}{\partial y_i}\right)^{(n)} = \frac{\Delta \xi^{(n)}}{\Delta y_i^{(n)}}$. If $\Delta y_i^{(n)}$ tends to 0, the slope tends to infinity thus representing an 'almost vertical side'. This model for the roughness elements can be used to evaluate the wavenumber transforms of the surface roughness involved in the function Θ. We also recall that experimental measurements

showed that the rough wall flow we are interested in does not vary significantly in the spanwise (y_3) direction. We can therefore choose any convenient (y_1, y_2) plane to perform our study. We will choose the observer location to be in the plane defined by $y_3 = 0$. We also consider an acoustically compact roughness patch, defined by $k_0 h << 1$. These two assumptions allow us to simplify the function Θ, reducing to the wavenumber transform of the rough surface in the y_1 direction only. Θ can eventually be expressed in a form independent of the wavenumbers and involving roughness characteristics only. Thus it can be taken out of the integration. Using the relationship between the wavenumber spectrum of the surface pressure and its power spectral density, the integral of Ψ_{PP} is shown to reduce to a constant. The final expression for the power spectral density of the far field pressure is given in (4.2.4) by:

$$\Phi_{pp}(x,\omega) \approx \Pi \left(\frac{x_1}{|x|} \right)^2 \frac{(k_0 h)^2 \Sigma S_{pp}(\omega)}{|x|^2} \tag{4.2.4}$$

with $\Pi = \dfrac{\alpha^2}{(2\pi)^2}$

α in the constant Π is a scaling factor of an order of 1, making Π a constant for every geometrically identical rough surfaces. Σ is the area of the roughness patch. h is the r.m.s. roughness height of the patch. The previous equation gives a simple formula for the acoustic far field spectrum emitted by the turbulent boundary layer over a rough wall as a function of the surface pressure spectrum at a single point, the planform area, the rough surface characteristics and the distance between the observer position and the source

location. A few assumptions were made to derive this formula such as the observer to be located in the acoustic far field, the wavelength to be large compared to the boundary layer thickness, the shear stresses to be negligible and the rough surface to be made of randomly distributed elements with almost vertical sides and falling into the category of the acoustically compact roughness.

Equation (4.2.4) is easily implemented in the code developed in the previous chapter. The power spectral density of the surface pressure being the output of chapter 3, it can be readily plugged in this equation. The observer position represents the location of the far field microphone used in the experiments and the source location, the point where the surface pressure spectrum was calculated. The constant Π is obtained by matching the measurements of the far field noise with the spectrum of the far field noise calculated from the measurements of the near field noise being used in equation (4.2.4). We find that is must be equal to 0.11 for the roughness we consider. The roughness patches used in the experimental setup have an area $\Sigma = 0.18605 m^2$.

4.3. Inclusion of the roughness

We recall that the CFD model used to obtain numerical values of the flow in chapter 2 did not include any roughness parameter. Meanwhile, the theory developed in this chapter to calculate the radiated noise of this turbulent flow is based on assumptions neglecting quadrupole order terms in Goldstein equation (4.1.1) with respect to the dipole order terms created by the interaction of the roughness elements with the flow.

This is addressed by considering a hydrodynamically smooth surface. If the roughness elements on the patches are small enough to remain within the viscous sublayer where the viscous forces are strong enough to maintain a laminar flow, the turbulences in the outer boundary layer do not interact with the roughness elements thus involving a flow on a virtually smooth surface, or hydrodynamically smooth surface. However, if the roughness elements do not influence the aerodynamic flow, they still have an impact on the acoustic radiated field. Figure 30 at the beginning of this chapter showed the three different effects roughness elements have on the surrounding turbulent flow; they enhance the existing turbulence, they increase the skin friction and they scatter the convected pressure waves. The first two phenomena do not occur anymore since the turbulent flow is not in contact with the patch. But the existing acoustic waves are always scattered whether the roughness elements are within the laminar sublayer or not. Curle (1955) showed that the acoustic field generated by this phenomenon is of dipole order, making the theory developed here valid even for a hydrodynamically smooth surface. We can always obtain aerodynamic and turbulence parameters by running a CFD model of the flow over a smooth surface and then assume a specific roughness height to conduct our acoustic calculations as long as this value stays within the range of the hydrodynamic smoothness. The viscous sublayer is defined in wall units by

$$y^+ = \frac{\rho_0 u_\tau d}{\mu} \leq 10 \tag{4.3.1}$$

ρ_0 being the density of the fluid, μ its dynamic viscosity, u_τ the friction velocity and d the distance from the wall. So we will consider in this study only rough surfaces whose r.m.s. height is small enough to verify equation (4.3.1). The following Table 1 gives the maximum value of d that verifies equation (4.3.1) for different nozzle velocities. Data was measured by Grissom *et al.* (2007).

Nozzle velocity U_{nozzle} (m/s)	$\frac{U_{\max}}{U_{nozzle}}$	$\frac{u_\tau}{U_{\max}}$	d (mm)
30	0.39	0.060	0.208
40	0.38	0.059	0.163
45	0.31	0.057	0.183
60	0.38	0.057	0.112

Table 1: value of d for different nozzle velocities

Table 2 below shows the characteristics of the different roughness patches that were tested experimentally.

Roughness type	Nominal height (mm)	RMS measured height (mm)
20Belt	0.95	0.207
36Belt	0.53	0.187
40Grit	0.425	0.156 to 0.133
60Grit	0.265	0.106
80Grit	0.19	0.066
100Grit	0.14	0.0412
150Grit	0.092	0.0287
180Grit	0.082	0.0245
220Grit	0.067	0.0173

Table 2: Roughness characteristics

Thus, for a given nozzle velocity, the patch with the highest acceptable roughness permitting the hydrodynamically smooth hypothesis can be found by matching the value of d to the values of r.m.s. height.

4.4. Results

In this paragraph we will give results for the far field pressure spectrum. The results of this study will be compared to the experimental measurements reported by Alexander (2009). The measurements were made using a microphone positioned in the far field at (1029,473,0)mm. Also we will use the surface pressure results established in the previous chapter for the surface location (1352,0,0)mm. Therefore, when the distance between the

source and the observer is needed, we will refer to these two locations. Attention will be focused on one type of roughness only, the difference between several values of roughness being small and a matter of a scaling factor. We will choose the case of 60Grit i.e. a rms roughness height of 0.106mm. This roughness fits in the range of hydrodynamically smoothness according to paragraph 4.3 and to the Table 1. Figure 31 presents the far field spectra obtained for different values of the parameter R.

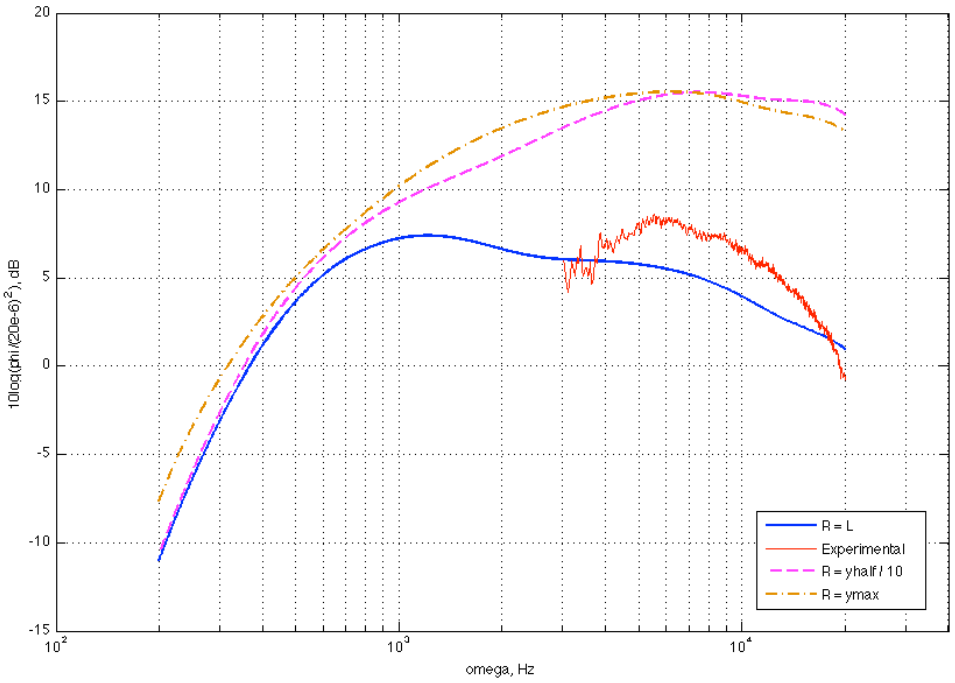

Figure 31: Far field pressure spectra for a roughness of 60Grit and for different values of the parameter R

Experimental data represents the subtracted spectrum, defined as the pressure recorded with the roughness patch in position on the plate minus the pressure recorded with the smooth plate alone. This explains the absence of noise in the frequencies below 3000Hz. The performances of the simulation of the far field pressure spectrum are comparable to

the modeling of the near field noise. Both cases are consistent to each other and to the experiments. The difference in amplitude here is about the same than in the near field case, less than 5dB for R=L and 7 to 15dB for the two other cases.

Similarly to section 3.3, we can observe the influence of the approximation of U'/U" on the far field pressure for the case R=L.

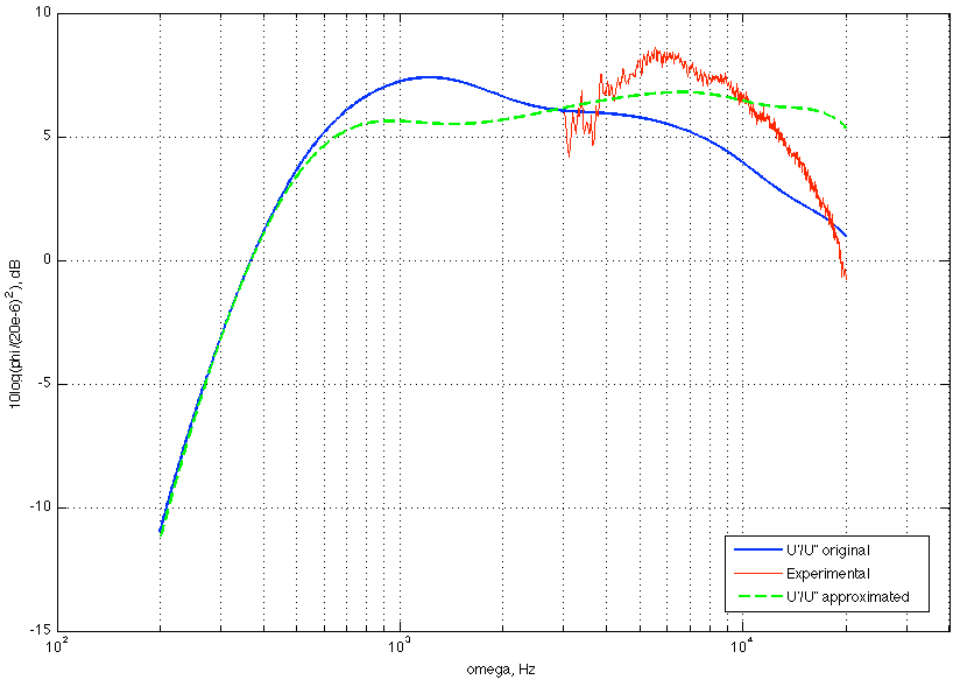

Figure 32: Far field pressure spectra for a roughness of 60Grit with and without the approximation of U'/U"

Again, the results are comparable to the near field case. The difference with and without the approximation of U'/U" is highlighted due to the shorter range of the amplitude of the spectra but there is still less than 5dB at 20kHz. We make the same observation that the case without the approximation of U'/U" seems to be in better agreement with the experiments. As it was explained in section 3.3, we don't make any conclusions on this

point without further knowledge on the influence of the resolution of the boundary region in the CFD study.

CHAPTER 5: CONCLUSIONS

This thesis aimed at reproducing the noise emitted by a turbulent boundary layer flow through the use of RANS calculations and by implementing a theory based on the representation of the turbulence kinetic energy by a superposition of vortex sheets of different amplitudes and uncorrelated with the distance to the wall.

The first conclusion drawn from this study is the critical importance of the accuracy of the CFD simulation, especially in the near-wall region. Although the numerical results appear to be in very good agreement with the aerodynamic measurements that were performed of this flow, the resolution of the numerical grid in the first few millimeters above the wall might require a refinement in order to perform better in the implementation of the associated theory.

Due to this potential lack of accuracy of the numerical simulation, assumptions had to be considered in the implementation of the theory. The resolution of the numerical model seems to have a direct impact on the calculation of the derivatives of U. Therefore, the eventual numerical inaccuracy was addressed by employing a theoretical model of the velocity profile of wall jets to calculate the derivatives of U. The validation of this hypothesis will be found in further numerical simulations, with an improved resolution.

The theory giving the surface pressure spectrum from a numerical calculation of the turbulence kinetic energy still includes areas that need further development such as the non-dimensional lengthscale involved in the calculation of the turbulence kinetic energy of the *w*-component of the velocity that is still uncertain. Several values were tested spanning a broad range and it appears that assuming this parameter to be equal to the turbulence lengthscale performs well.

The study finally proved that it is possible to reproduce the pressure spectrum on the surface and in the far field with an accuracy of less than 5dB and with a spectrum shape that satisfactorily fits the measurements at high frequency. This is a good achievement regarding the numerous errors that add up to the final result all along the process. That allows us to conclude that the two theories that were used in this study to calculate the pressure spectrum in the far field provide coherent and satisfactory results. The theory developed to predict the noise radiated by the trailing edge of an airfoil seems to apply to other types of flows.

In the continuity of the work presented here, further CFD calculations with a higher level of accuracy should be the most important task to accomplish. The resolution of the boundary region would have to be improved by at least a factor of ten in almost all the boundary layer thickness. Attention must be focused on having fine and smooth transitions between the layers of cells, with an aspect ratio as close to 1 as possible. This will allow to make conclusions on which profile of U'/U" considered in the study is the closest to the reality. Finally, a simulation in three dimensions would permit to verify the empirical observation that the flow is two-dimensional in the central region of the plate.

However, this simulation might face a considerably larger size of grid if the current geometry is conserved.

NOMENCLATURE

Roman

A	Vortex sheet strength function
a_s	Amplitude of the vortex sheets
C	Defined in (3.1.8)
c_∞	Speed of sound
E	Turbulence energy spectrum
$E[x]$	Expected value of x
F	Defined in (3.2.3)
f_i	Surface force per unit area
G	Green function
h	r.m.s. roughness height
k	Turbulence kinetic energy (CFD value)
k_0	$\frac{\omega}{c_\infty}$, acoustic wavenumber
k_i	Wavenumber in the *i-th* direction
L	Local turbulence lengthscale
M	Mach number
N	Number of roughness elements
n_i	Unit vector normal to the surface
P	Mean pressure
P_e	Defined in (3.1.12)
P_k	Production of k
p	Pressure fluctuation
p_s	Surface pressure fluctuation
Q_s,Q_w	Defined in (3.2.1)
q,q_s,q_w	Turbulence kinetic energy
Re	Reynolds number
R	Non-dimensional lengthscale
S_{aa}	Wavenumber spectrum of the amplitude of the vortex sheets
S_{ij}	Viscous stress tensor

$S_{pp}(k_1,k_3,\omega)$	Wavenumber spectrum of the surface pressure
$S_{pp}(\omega)$	Power spectral density of the surface pressure
s_i	s-component of the velocity
$\overline{s}_i$	Non-dimensional s-component of the velocity
U	U_2, mean velocity in the x_2 direction
U',U''	Derivatives of U with respect to x_2
U_i	$U(x_i)$, mean velocity
U_0	$-\frac{\omega}{k_1}$, convection velocity
$U_{\max}$	Maximum velocity
U_∞	Scaling velocity
u	v_2, velocity fluctuation in the x_2 direction
u',u''	Derivatives of u with respect to x_2
u_τ	Friction velocity
V_n	Velocity component normal to the surface
v_i	Velocity fluctuations
$\hat{v}_i$	Fourier transform of v_i
$\tilde{v}_i$	Instantaneous value of v_i
w_i	w-component of the velocity
$\overline{w}_i$	Non-dimensional w-component of the velocity
x	Observer location
$\lvert x\rvert$	Distance between source and observer
x_i	(x_1,x_2,x_3), Coordinate system
y	Source location
y_i	$(y_1,y_2,y_3)=(x_1,x_2,x_3)$, Coordinate system
y_0	Solution of $U(y_0)=U_0$
y^+	Wall unit

Greek

α	Roughness geometry scale factor
δ_0	Scaling distance
ε	Turbulence dissipation rate
$\Phi_{pp}(x,\omega)$	Power spectral density of the far field pressure
Γ	Defined in (3.1.5)
λ	$\sqrt{k_1^2+k_3^2}$, wavelength
λ_0	$\sqrt{\frac{\omega^2}{U_0^2}+k_3^2}$
μ	Dynamic viscosity

μ_t	Eddy viscosity
Π	Roughness geometry scale factor
$\Theta(k_1,k_3,\omega)$	Roughness filter spectrum
ρ	Fluid density fluctuations
ρ_0	Mean fluid density
Σ	Planform area, projection of ξ on the plane (y_1,y_3)
ω	Angular frequency
ω_i	Vorticity fluctuations
$\omega_i^{(s)}$	Vorticity of the s-component
ξ	Surface height
$\psi_j,\overline{\psi}_j$	Vector potentials
$\Psi_{PP}(k_1,k_3,\omega)$	Normalized wavenumber spectrum of the surface pressure
$\zeta^{(j)}$	Wavenumber transform of the roughness height ξ

REFERENCES

Alexander, W.N. (2009), "Normalization of roughness noise on the near-field wall pressure spectrum", *MS thesis*, Virginia Tech.

Calvetti, D., Golub, G.H., Gragg, W.B., Reichel, L., (2000), "Calculation of Gauss-Kronrod of quadrature rules", *Mathematics of computation*, vol. 69, pp 1035-1052.

Cole, L. D. (1980), "Measurements of sound generated by boundary-layer turbulence over smooth and rough surfaces", *DTNSRDC report* SAD-288E-1942.

Curle, N. (1955), "The influence of solid boundaries upon aerodynamic sound", *Proc. Roy. Soc. A.* 231, pp. 505-514, (doi:10.1098/rspa.1955.0191).

George, W. K., Abrahamsson, H., Eriksson, J., Karlsson, R. I., Lofdahl, L. and Wosnik, M. (2000), "A similarity theory for the turbulent plane wall jet without external stream", *Journal of Fluid Mechanics,* vol. 425, pp. 367-411.

Glegg, S. and Devenport, W. (2009), "The far field sound from boundary layers noise", *Proc. R. Soc. A*., RSPA 2008.0318—14/2/2009—20:11—PARANDAMAN—327269— pp. 1–19.

Glegg, S., Morin, B., Atassi, O. and Reba, R. (2008), "Using RANS calculations of Turbulent Kinetic Energy to provide predictions of trailing edge noise", *AIAA 2008-2993 (To be published).*

Goldstein, M. (1976), "Aeroacoustics", New York, NY: McGraw Hill.

Grissom, D. L., Devenport, W. J., Smith, B. S., and Glegg, S. L. (2007), "Rough-wall boundary layer noise: an experimental investigation", *AIAA 2007-3418.*

Howe, M. (1984), "On the generation of sound by turbulent boundary layer flow over a rough wall", *Proc. Roy. Soc. A.* 395, pp. 247-263, (doi:10.1098/rspa.1984.0100).

Kronrod, A.S. (1965), "Nodes and weights of quadrature formulas", New York: Consultants Bureau (Authorized translation from the Russian).

Lee, Y-T., Blake, W.K., Farabee, T.M. (2005), "Modeling of a wall pressure fluctuations based on time-mean flow field", *Journal of Fluids Engineering*, vol. 127, pp. 233-240.

Lighthill, M. J. (1952), "On sound generated aerodynamically" 1. General theory., *Proc. R. Soc. A.* 211, pp. 564-587, (doi:10.1098/rspa.1952.0060).

Liu, Y, Dowling, A. P. and Shin, H. (2006), "Effect of surface roughness on airframe noise", *AIAA 2006-2510*.

Mathey, F. (2007), "Aerodynamic noise simulation of the flow past an airfoil trailing-edge using a hybrid zonal RANS-LES", *Computers & Fluid*, vol. 37, pp. 836-843.

Moser, R. D., Kim, J. and Mansour, N. N. (1998), "Direct Numerical Simulation of turbulent channel flow up to Re=590", *Physics of fluids,* vol.11, pp. 943-945.

Peltier, L.J, Hambric, S.A. (2007), "Estimating turbulent boundary layer spectra from CFD RANS solution", *Journal of Fluids and structures*, vol. 23, pp. 920-937.

Pope, S.B. (2000), "Turbulent flows", *Cambridge University Press.*

Spitz, N. (2005), "Predictions of trailing edge noise from two-point velocity correlations", *MS thesis,* Virginia Tech.

Townsend, A.A, (1978), "The structure of turbulent shear flow", *Cambridge University Press.*